Parametric Subharmonic Instability and the β-effect

by

Ian Chan

B.Sc., University of British Columbia, 2007

A THESIS SUBMITTED IN PARTIAL FULFILLMENT OF

THE REQUIREMENTS FOR THE DEGREE OF

Master of Science

in

THE FACULTY OF GRADUATE STUDIES

(Mathematics)

The University of British Columbia

(Vancouver)

August 2010

Abstract

Parametric subharmonic instability (PSI) is a nonlinear interaction between a resonant triad of waves, in which energy is transferred from low wavenumber, high frequency modes to high wavenumber, low frequency modes. In the ocean, PSI is thought to be one of the mechanisms responsible for transferring energy from M_2 internal tides (internal gravity waves with diurnal tidal frequency) to near-inertial waves (internal gravity waves with frequency equal to the local Coriolis frequency) near the latitude of $28.9°$. Due to their small vertical scale, near-inertial waves generate large vertical shear and are much more efficient than M_2 internal tides at generating shear instability needed for vertical mixing, which is required to maintain ocean stratification.

The earlier estimate of the time-scale for the instability is an order of magnitude larger than the time-scale observed in a recent numerical simulation (MacKinnon & Winters, 2005) (MW). An analytical model was developed by Young *et al.* (2008) (YTB), and their findings agreed with the MW estimation; however as YTB assumed a constant Coriolis force, the model cannot explain the intensificaiton of PSI near $28.9°$ as observed in the model of MW; in addition, the near-ineartial waves can propagate a significant distance away from the latitude of $28.9°$.

This thesis extends the YTB model by allowing for a linearly varying Coriolis parameter (β-effect) as well as eddy diffusion. A linear stability analysis shows that the near-inertial wave field is unstable to perturbations. We show that the β-effect results in a shortening in wave length as the near-inertial waves propagate south; horizontal eddy diffusion is therefore enhanced to the south, and limits the meridional extent of PSI. The horizontal diffusion also affects the growth rate of the instability. A surprising result is that as the horizontal diffusion vanishes, the system becomes stable; this can be demonstrated both analytically and numerically.

Mathematically, the β-effect renders the spatial differential operator nonnormal, which is characterized with the aid of pseudo-spectra. Our results suggest the possibility of large amplitude transient growth in near-inertial waves in regimes that are asymptotically stable to perturbations.

Contents

List of Figures

Acknowledgements

First and foremost, I would like to thank my supervisor Neil Balmforth for being an inspiring mentor over the last three years. It has been a pleasure working with him and I have learnt a great deal from him, which will no doubt be invaluable to my career. I would also like to thank Kraig Winters and Bill Young for their comments for this manuscript.

Navigating myself through the degree would've been much more difficult without the help from the faculty members at UBC. I would like to thank Douw Steyn, Philip Loewen, Eric Cytrynbaum, Mark Maclean, George Bluman, and Richard Anstee for their constant guidance, which helped me grow immensely in my research and teaching.

I would also like to thank the staff of the Department of Mathematics and the Institude of Applied Mathematics, especially Lee Yupitan for answering the countless administrative questions I had and Marek Labecki for his help on solving computer related issues.

Finally I would like to thank my family for their support during my studies. I would like to thank my wife Giorgia especially for her constant encouragements and love.

Chapter 1

Introduction

The ocean is constantly covered by waves, which can range from small ripples generated by a gentle breeze, to giant rogue waves found in storms. These waves exist due to gravity: if the water surface is perturbed upwards, gravity will act on the water to pull the surface downwards to restore the surface back to its equilibrium; however most often it will overshoot, causing a depression to form, and gravity will now act on the water surrounding the depression to fill in the depression. This sequence will occur repeatedly, which results in the familiar waves we observe on the ocean surface.

Gravity waves are not confined to surface of the ocean, as they also exist underneath the surface. Due to differences in temperature and salinity, the density in the ocean typically increases with depth, and therefore when a parcel of water is perturbed downwards, the denser ambient fluid provides a positive buoyancy that acts as a restoration force. The resulting waves are called internal gravity waves (IGWs), and these waves are characterized by the up and down motion of isopycnal (constant density) surfaces.

These internal gravity waves have several features that differ from their coun-

terparts on the surface. Firstly, the sharp density contrast between air and water results in a much higher frequency of oscillation for the surface waves; the typical time scale for surface waves observed near a beach is measured in seconds. In contrast, the restoration force for IGWs is provided by a more gentle density gradient, and the frequency of vertical oscillations can be characterized by the Brunt-Väisälä frequency N:

$$N = \sqrt{-\frac{g}{\rho_0}\frac{d\rho}{dz}}, \tag{1.1}$$

where g is the gravitational acceleration, ρ_0 is the characteristic density, and z is the vertical coordinate. Below the 'mixed layer' on the surface of the ocean, which is uniform in density and extends up to 50m, the buoyancy frequency decreases from $10^{-2}s^{-1}$ to about $10^{-4}s^{-1}$ in the deep ocean (about 4000m) (Thorpe, 2005); these frequencies correspond to time-scales ranging from minutes to hours.

The IGWs also have a much larger spatial scale compared to surface gravity waves. For example the internal waves associated with the diurnal tide can span the entire depth of the ocean ($10^3 m$), while having horizontal scales measured in tens of kilometres, which is in stark contrast to surface waves that typically have heights of $0.1 - 10m$ and horizontal wavelengths of perhaps a tens of meters. A consequence of the large horizontal scale of IGWs is that IGWs are susceptible to the Coriolis effect, which is reflected in the dispersion relation:

$$\frac{k^2 + l^2}{m^2} = \frac{\omega^2 - f^2}{N^2 - \omega^2} \tag{1.2}$$

which stipulates a relationship between $(k, l, m) \equiv \vec{k}$ (the wavenumbers in the x, y, and z direction respectively[1]), and the frequency of the wave ω. f denotes the Coriolis parameter, which depends on the earth's rate of rotation ($\Omega = 7.27 \times$

[1]Throughout this thesis we will adhere to the convention in oceanography by orienting the positive $x-$axis towards east, positive $y-$axis towards north, and positive $z-$ upwards

2

$10^{-5}s^{-1}$) and latitude (ϕ):

$$f = 2\,\Omega \sin \phi. \tag{1.3}$$

Since the wavenumbers are real, and $N \gg f$ in general, an implication of (1.2) is that an IGWs can only exist if $N \geq \omega \geq f$. In addition one can use (1.2) to show the direction of the group velocity makes an angle of α with the horizontal plane, where α satisfies:

$$\tan \alpha = \sqrt{\frac{k^2 + l^2}{m^2}} = \sqrt{\frac{\omega^2 - f^2}{N^2 - \omega^2}}. \tag{1.4}$$

Since the energy propagates along the direction of the group velocity, this shows that in general IGWs transports energy both in the horizontal and vertical direction, which is in contrast to the surface waves where energy is propagated along the surface. Two limiting cases can be considered:

1. $\omega \to N$: in this case the angle of propagation tends to $90°$, which corresponds to vertical oscillations with frequency N.

2. $\omega \to f$ (The near-inertial limit): in this limit the angle of propagation tends to 0, and energy is propagated horizontally. In addition, as the RHS of (1.2) vanishes as $\omega \to f$, m^2 must be large relative to $k^2 + l^2$ in order for the equation to hold. Since the wave number are inversely proportional to the spatial scale, this implies that the vertical scale m^{-1} must become small compared to the horizontal scale $(k^2 + l^2)^{-1/2}$.

1.1 IGWs and the dynamics of the ocean

As warm water has a lower density than cold water, the constant heating at the surface will in principle result in a warm layer near the surface, and the rest of the ocean will consist of cold dense water underneath. In reality the density profile is

much smoother due to mixing, and one can find circulations that span the entire depth of the ocean (the thermo-haline circulation for example). Molecular diffusion itself cannot account for the mixing, as the diffusivity of heat and salt are in the order of $10^{-6} - 10^{-7} m^2 s^{-1}$, while the diffusivity needed to maintain the stratification is estimated to be $10^{-4} m^2 s^{-1}$ (Munk & Wunsch, 1998). It is believed that the breaking of internal waves is responsible for the turbulence, and the diapycnal (across density surfaces) mixing that follows (Laurent & Garrett, 2002).

Munk & Wunsch (1998) estimated that 2.1TW of energy is needed to maintain the stratification in the abyssal ocean via mixing; as an additional 2.6TW of energy is dissipated through turbulence mixing in the shallow oceans, a total energy source of 4.7TW needed. Wind induced mixing, either directly near the surface, or indirectly via the excitation of geostrophic motions and internal gravity waves, provides 1.2TW of energy. The remaining 3.5TW is supplied by the various modes of tides due to the sun and the moon; amongst the modes, the semi-diurnal component of the lunar tide (denoted by M_2) is the dominate source, accounting for 2.5TW.

The effect of the moon's gravity field on the earth is not uniform everywhere on the surface, and the minute difference is sufficient to cause a deformation in the ocean: the result is that the ocean bulges out along the earth-moon axis, both towards and away from the moon. As the earth rotates around its axis, a point on the surface over the ocean will experience a rise and a subsequent fall in the sea-level as it passes through a bulge. As most locations will pass through both bulges, the result is the semi-diurnal tide that occurs approximately twice daily, or every 12 hours and 25 minutes.

Since the earth's rotation rate $(7.292 \times 10^{-5} s^{-1})$ is much higher than the rate at which the moon orbits around the earth $(2.662 \times 10^{-6} s^{-1})$, we can view the earth

as a sphere moving through a viscous film of fluid held in place by the gravity of the moon. The friction between the earth and the ocean causes the earth's rotational rate to slow down, as well as a misalignment of the tidal bulge along the moon-earth axis. The misalignment in turn imparts a torque on the moon, causing it to gain rotational momentum and increase its distance from the earth. The rotational energy is partially dissipated in the ocean, and partially transferred into the orbital energy of the moon, causing it to move further away from the earth. The modern value of lunar recession, obtained via laser ranging, is determined to be 3.82 cm/year (Dickey *et al.*, 1994), which corresponds to a tidal dissipation rate at 2.5 TW (Munk & Wunsch, 1998).

Tidal dissipation in the ocean

The subject of tidal dissipation can be dated back to Sir G.I. Taylor (1920) and Sir Harold Jeffreys (1921). Taylor estimated the the frictional dissipation over the Irish sea alone to be 0.051 TW, while Jeffreys estimated the global dissipation over shallow seas to be 1.1 TW; later Miller (1966) pegged the value at 1.6TW, while recent values inferred by satellite data is for the M_2 mode is 1.8TW (Egbert, 1997; Munk & Wunsch, 1998). The discrepancy between the estimated dissipation over shallow seas and the total dissipation calculated from astronomical data can be attributed to the excitation of internal gravity waves due to bottom topography in the deep ocean. While the conversion over continental shelves is long known, the conversion over deep ocean has been thought to be insignificant until recently (Garrett, 2003). Part of the reason for the revision is due to the availability of satellite altimetry data, which suggests that dissipation over the deep ocean is responsible for converting 1TW of energy (Egbert & Ray, 2000, 2001).

The mechanism behind the tidal conversion is simple: as the tide moves around the earth, the water in the ocean is moved back and forth; in the presence of submarine ridges, the density surfaces are perturbed and internal gravity waves are launched in a fashion similar to lee waves generated by mountains. These internal gravity waves (called internal tides) then propagate from the bottom up into the open ocean, carrying energy upwards that ultimately leads to overturning and mixing (Garrett, 2003). These internal tides can be observed with the aid of satellite altimetry: for example, Ray & Mitchum (1997) reported internal tides propagating away up to 500km away from the Hawaiian Islands, primary as mode-1 baroclinic tide. The baroclinic tides often have the same frequency as the underlying barotropic tide due to the weak background tidal current (Garrett & Kunze, 2007), while the horizontal structure is around 20-100km (Laurent & Garrett, 2002). The Richardson number for these internal tides exceeds unity, suggesting that the internal tide cannot lead to overturning directly; it is believed that energy is cascaded down via non-linear wave-wave interaction into smaller scale internal waves, which are more effective at causing over-turnings (Laurent & Garrett, 2002)..

Non-linear wave interactions in internal gravity waves are thought to be responsible for shaping and maintaining the energy spectra of internal waves in the open ocean into the so-called Garrett-Munk (GM) spectrum (Müller *et al.*, 1986; Thorpe, 2005). Garrett & Munk (1972, 1975) proposed a model for the observed energy spectra of internal waves that is in remarkable agreement with experimental data from different sites; this suggests that there is a single universal mechanism responsible for cascading energy from large scale motion to small scale mixing. As abyssal mixing is an essential component to the dynamics of large scale ocean circulations that in turns play a pivotal role in our climate, the GM spectrum and

6

ocean mixing have received plenty of attention over the last forty years.

Non-linear wave interactions have been explored theoretically since the 1960's. Phillips (1960, 1961) considered two waves with frequencies and wave-numbers $(\omega_1, \vec{k}_1)$ and $(\omega_2, \vec{k}_2)$, and considered a third mode whose frequency and wave-number satisfy the resonance condition:

$$\omega_1 \pm \omega_2 = \omega_3 \,, \tag{1.5}$$

$$\vec{k}_1 \pm \vec{k}_2 = \vec{k}_3 \,. \tag{1.6}$$

In this case, the third wave will be forced resonantly, and energy is transfered from the first two modes into the third. Bretherton (1964) considered the interaction between a triad of discrete modes, where $\omega_1 + \omega_2 = \omega_3$ and $\vec{k}_1 + \vec{k}_2 = \vec{k}_3$, and provided a heuristic argument for the evolution equation of the amplitudes a_i:

$$i\omega_1 \frac{\partial a_1}{\partial t} = \hat{D} a_2^* a_3 \,, \tag{1.7}$$

$$i\omega_2 \frac{\partial a_2}{\partial t} = \hat{D} a_1^* a_3 \,, \tag{1.8}$$

$$i\omega_3 \frac{\partial a_3}{\partial t} = \hat{D} a_1 a_2 \,, \tag{1.9}$$

where $\hat{D}$ is a real coefficient that describes the interaction, and generally depends on the wave-numbers. Hasselmann (1966, 1967) studied weak non-linear wave interaction for a continuous field of waves that is assumed to be Gaussian and statistically stationary ('the random phase hypothesis'). McComas & Bretherton (1977) used a similar method to investigate the resonance interaction in the GM spectrum; they numerically computed the energy transfer in the spectrum, and concluded that the process is dominated by three classes of interactions: induced diffusion, elastic scattering, and parametric subharmonic instability. For Induced diffusion, wave action (wave energy divided by frequency) diffuses from a high-frequency, high-wavenumber

7

mode to one that has similar frequency and wavenumber. Elastic scattering occurs between two high frequency modes, with similar horizontal wave numbers but opposite vertical wave number; in this case there is rapid energy transfer between the two high frequency modes leaving the third low frequency mode largely unchanged. The last class of interaction is parametric subharmonic instability (PSI), where a large scale wave decays into two small scale waves with half the frequency. An important observation is that among the three pathways PSI is the only mechanism where energy is transferred into waves with a much different wave number. For a thorough discussion, please see McComas & Bretherton (1977) or Müller et $al.$ (1986).

1.2   Parametric subharmonic instability

Parametric subharmonic instability allows a wave to spontaneously excite daughter waves with higher wave numbers with half the frequency; it is a special case of (1.5) where $\omega_1 = \omega_2 = \omega_3/2$. Since the semi-diurnal internal tide has frequency angular frequency $M_2 = 2\pi/12.42\,hr = 1.405 \times 10^{-4}s^{-1}$, the daughter waves will have frequency $\omega = M_2/2 = 7.026 \times 10^{-5}s^{-1}$. As mentioned earlier, internal gravity waves can exist only if the frequency is greater than the local Coriolis frequency; thus for the daughter waves to exist, the latitude must satisfy the inequality $M_2/2 \geq 2\Omega \sin\phi$, or $\phi \leq 28.9°$. The implication is that PSI can only occur between the equator up to the critical latitude $28.9°$. At the critical latitude the daughter waves have frequency that is equal to the local Coriolis frequency, and therefore they are near-inertial oscillations (NIO).

While PSI have received some attention over the 1970's, the interest waned as it was believed that the energy transfer via PSI occurs over a time-scale of 100 days for the mode-1 internal tide, which is too slow compared to other processes to

remove energy efficiently (Olbers & Pomphrey, 1981); however the interest in PSI have been renewed in recent years due to several new studies. Hibiya *et al.* (1998, 2002) carried out a set of numerical experiments, where a quasi steady internal wave field was perturbed by injecting energy into the first vertical mode at the M_2 freqency. For the experiment at 49°N, the spectra did not differ significantly over 10 inertial period; on the other hand, the energy was quickly transfered to the high wave-number modes in the $f < \omega < 2f$ range within 10 inertial periods at 28°N.

MacKinnon & Winters (2005) (henceforth MW) solved the full 3-D equation of motions numerically with a linearly stratified background; a mode-1 internal tide was excited at the southern boundary, which propagated northward in the presence of background noise. After the initial spin-up, instabilities started to develop near the critical latitude. The instability had much finer vertical structure compared to the mode-1 internal tide, and a plot of temporal spectra plot reveals a high spectral content over the $M_2/2$ frequency. At the same time the energy flux associated with internal tide decreased by 62.5% as it crossed the critical latitude. In addition the time scale of the energy transfer was estimated to be 10 days, which was an order of magnitude smaller than the estimation of Olbers & Pomphrey (1981). MW attributed the disparity to the fact that the estimation of Olbers & Pomphrey was based on the random phase assumption, but from the numerical simulation the interaction were clearly much more coherent. The efficiency of PSI led the authors to describe this as the 'subtropical catastrophe'. Simmons (2008) ran a global ocean model with realistic geometry, and observed energy transfer into the $M_2/2$ modes near the critical latitude as well. A longitudinal cross section near a internal tide generation site showed that PSI intensified near the surface, possibly due to the non-linear stratification.

Recent field measurements also pointed to the presence of PSI activity in the ocean. For example, Rainville & Pinkel (2006) compared the vertical profiles at a site near Hawaii with strong internal tide activity (nearfield) to a site that is further away, and found a strong link between the semi-diurnal energy flux at the nearfield site and the diurnal energy flux at the farfield site; this suggested that as the internal tide radiates away from the generation site it transfers energy down to the diurnal mode via PSI. Carter & Gregg (2006) came to a similar conclusion based on another set of data from the Hawaii area. Through a bicoherence analysis they were able to demonstrate that the strength of the $M_2/2$ diurnal mode was correlated to the strength of the M_2 internal tide. Alford *et al.* (2007) estimated the reduction in energy flux as the internal tide crosses the critical latitude to be 10-20%, which is significantly smaller than the 62% in MW; they suggested that the presence of higher modes de-tuned the resonance and leads to a reduction in efficiency.

Young *et al.* (2008) (henceforth YTB) constructed an analytical model based on a multiple time scale approach, where the time scale over which evolution of the PSI instability takes place was slower than the inertial time scale f^{-1}. With this assumption the Boussinesq equations were simplified into a PDE that describes the evolution of the PSI wave. For simplicity the latitude was restricted to the critical latitude $28.9°$, so that the daughter waves are near-inertial. The stability of a plane wave internal tide in a linearly stratified ocean was considered, and using realistic parameters the growth rate of the unstable near-inertial mode agreed with MW in order of magnitude. YTB also considered the stability problem in a more realistic density stratification; using Gill's model for the ocean stratification, the most unstable normal modes for the near-inertial field were found to be concentrated just under the mixed layer.

10

1.3 Goals

The goal of this thesis is to expand on the model of PSI derived by YTB; in particular we will allow the Coriolis force to vary with latitude, and assess its effect on PSI. The rational behind this modification is that over the time-scale for PSI (10 days), there is significant propagation of the near-inertial waves, and thus the constant Coriolis parameter assumption may not be justified. In addition, we would like to investigate the effect of dissipation to determine if it is crucial to the instability, in particular to the understanding to vertical scale selection that appeared in the numerical simulations.

Chapter 2

Mathematic Description of PSI

A familiar example of resonance occurs when a simple harmonic oscillator is forced at its natural frequency. Here we will first consider the following equation, which describes an oscillator forced by a weak ($\epsilon \ll 1$) periodic driver with frequency 2:

$$y'' + \omega^2 y = \epsilon\, y^*\, e^{2it}. \tag{2.1}$$

The presence of y^* (the complex conjugate of y) in the forcing term indicates that the forcing is moderated by feedback from the oscillator. Since the natural frequency for the oscillation is $\pm\omega$, the homogenous solutions are $e^{i\omega t}$ and $e^{-i\omega t}$. These two solutions will result in forcing terms that are proportional to $e^{i(2-\omega)t}$ and $e^{i(2+\omega)t}$ respectively on the RHS of (2.1). As long as $\omega \neq 1$, the forcing will be at a frequency that differs from the natural frequency, and hence no resonance will occur.

On the other hand, when $\omega = 1$ both the homogenous solution and the corresponding forcing will contain e^{it}, and in this case resonance will occur. One can analyse (2.1) through a multiple time scale approach. As the coupling is weak due to the small parameter ϵ, we would expect the amplitude of y to grow over a slow time scale $T = \epsilon t$. If we seek an ansatz to (2.1) of the form $y(t, T) = A(T)e^{i(t-\pi/4)}$,

we will have:

$$2i\epsilon A'(T)e^{i(t-\pi/4)} + O(\epsilon^2) = \epsilon A(T)e^{i(t+\pi/4)}, \tag{2.2}$$

Equating the $O(\epsilon)$ terms leads to a differential equation for $A(T)$:

$$\frac{dA}{dT} = \frac{1}{2}A \tag{2.3}$$

The above equations can be considered as a toy model for PSI, as the natural frequency of the oscillator is half the frequency of the driver, and therefore the resonant condition $\omega_1 + \omega_2 = \omega_3$ (where $\omega_1 = \omega_2 = \omega/2$) is satisfied. In addition the model predicts that the amplitude of $y(t)$ will grow as $e^{\epsilon t}$, indicating that the driver is transferring energy into the oscillator, and the amplitude grows exponentially over the slow timescale.

With this example in mind, we will now derive the model equations for PSI. The PSI model we will be using here is identical to the one derived by Young *et al.* (2008) except for two modifications. The first is the inclusion of the latitudinal dependence of the Coriolis force via a linearization of the Coriolis parameter $f = f_0 + \beta y$. In addition, we will include dissipation into our model, which was not considered by Young *et al.* As these two modifications can be easily included in the rigorous asymptotic derivation of the governing equations outlined in Young *et al*, we will not repeat the derivation here; instead we will take a more heuristic approach by assuming *a priori* that the PSI modes will have frequency $M_2/2$, and derive the governing equations.

2.1   Derivation of the PSI model

The starting point is the hydrostatic Boussinesq equations linearized around the background flow fields (U, V, W, B, P), which denote the velocities, buoyancy, and

pressure respectively. Since we are interested in the PSI in a mode-1 internal tide with frequency $2f_0 = M_2$, the background fields will be proportional to e^{-2if_0t} and have amplitudes depending only on the spatial coordinates (x, y, z), which respectively denote the coordinates in the east-west, north-south, and vertical directions. Notice that our model is not a complete triad resonance, since the amplitudes of the background fields are time independent, and do not diminish as energy is being extracted from the internal tide. It can be viewed as a linearized model for the triad resonance, where the amplitudes of the daughter waves are small, and therefore the feedback on the internal tide (also referred to as the 'pump wave') can be neglected. With (u, v, w, b, p) denoting the perturbations associated with the NIO, we have:

$$u_t + Uu_x + Vu_y + Wu_z + uU_x + vU_y + wU_z - fv + p_x + \mu(-\nabla^2)^n u = 0, \quad (2.4)$$

$$v_t + Uv_x + Vv_y + Wv_z + uV_x + vV_y + wV_z + fu + p_y + \mu(-\nabla^2)^n v = 0, \quad (2.5)$$

$$-b + p_z = 0, \quad (2.6)$$

$$u_x + v_y + w_z = 0, \quad (2.7)$$

$$b_t + Ub_x + Vb_y + Wb_z + uB_x + vB_y + wB_z + wN_0^2 = 0, \quad (2.8)$$

where $\nabla^2 = \partial_x^2 + \partial_y^2 + \partial_z^2$. The last terms in (2.4) and (2.5) describe the dissipative process, and the exponent $n = 0, 1, 2$ corresponds to the linear drag, eddy diffusion, and hyperdissipation model respectively. In the ocean, the presence of stratification implies that the turbulence is not necessarily isotropic, and horizontal mixing occurs much more readily than mixing vertically due to stable vertical stratification. For example, the measured eddy horizontal diffusivity in a dye-release experiment in open ocean ranged from 10^{-2} to $10^3 m^2 s^{-1}$ depending on the scale (Ledwell *et al.*, 1998), while the vertical eddy diffusivity is of the order of $10^{-5} m^2 s^{-1}$ (Ledwell *et al.*, 1993, 1998); therefore in the eddy diffusion model, the dissipation term is split into

14

its vertical and horizontal components:

$$\mu(-\nabla^2)^n u = \mu_H(-\nabla_H^2)^n u + \mu_V(-\partial_{zz})^n u, \tag{2.9}$$

where $\nabla_H^2 = \partial_x^2 + \partial_y^2$, and μ_H and μ_V are the horizontal and vertical eddy diffusivity respectively. We will ignore the diffusion of buoyancy b.

We can further simplify the equations using the assumptions stated in YTB. Since the background flow has a much larger vertical scale, any z-derivatives of the background variables can be ignored in (2.4) and (2.5). YTB assumed the buoyancy perturbations to be small compared to N^2, and therefore the coupling terms (product of pumpwave and near-inertial variables) in (2.8) are small compared to wN^2, and it will be the time derivative b_t providing the balance in (2.8). Introducing the complex variables

$$\mathcal{U} = u + iv, \quad \xi = x + iy, \tag{2.10}$$

the horizontal derivatives can then be written as:

$$\partial_\xi = \frac{1}{2}(\partial_x - i\partial_y), \quad \partial_{\xi^*} = \frac{1}{2}(\partial_x + i\partial_y). \tag{2.11}$$

We can then simplify (2.4) to (2.8) to:

$$\mathcal{U}_t + U\mathcal{U}_x + V\mathcal{U}_y + W\mathcal{U}_z + (U_x + iV_x)u + (U_y + iV_y)v$$
$$+ if\mathcal{U} + 2p_{\xi^*} + \mu_H(-\nabla_H^2)^n\mathcal{U} + \mu_V(-\partial_{zz}^2)^n\mathcal{U} = 0, \tag{2.12}$$

$$-b + p_z = 0, \tag{2.13}$$

$$u_x + v_y + w_z = 0, \tag{2.14}$$

$$b_t + wN_0^2 = 0. \tag{2.15}$$

Since PSI primarily transfers energy to waves with half the frequency, we seek oscillatory solutions with frequency f_0; more specifically, we will assume that the

15

solutions are of the form:

$$\mathcal{U} = \mathsf{L}\mathcal{A}(x, y, z, t)e^{-if_0 t}, \tag{2.16}$$

where $\mathsf{L} = \partial_z f_0^2 N^{-2} \partial_z$. The other near-inertial fields can then be obtained from (2.13) to (2.15):

$$w = -f_0^2 N^{-2} \mathcal{A}_{\xi z} e^{-if_0 t} + c.c., \tag{2.17}$$

$$b = if_0 \mathcal{A}_{\xi z} e^{-if_0 t} + c.c., \tag{2.18}$$

$$p = if_0 \mathcal{A}_\xi e^{-if_0 t} + c.c. \tag{2.19}$$

It is worth noting that while obtaining b though (2.15), we have made use of the assumption that the near-inertial period f_0^{-1} is much larger than the time scale on which b evolves, and the variation of the amplitude can be ignore. b can then be obtained by integrating wN^2 with respect to time. We will also linearize the Coriolis parameter f around the critical latitude:

$$f = f_0 + \beta y. \tag{2.20}$$

Once the pressure p is found, it can be substituted, together with the expression of $\mathcal{U}$ into (2.12). The first term in (2.12), $\mathcal{U}_t$, becomes:

$$\mathcal{U}_t = -if_0 \mathsf{L}\mathcal{A}e^{-if_0 t} + \mathsf{L}\mathcal{A}_t e^{-if_0 t}. \tag{2.21}$$

The main contributors to the slower tendency $\mathsf{L}\mathcal{A}_t$ arise from the terms that have the same phase (otherwise there are rapid cancellations over the diurnal cycle) i.e. the resonant terms. The others, referred to as non-resonant terms (NRT) can then be discarded. Among the coupling terms, only $(U_x + iV_x)u + (U_y + iV_y)v$ are resonant:

$$(U_x + iV_x)u + (U_y + iV_y)v = \tfrac{1}{2}\mathcal{U}(U_x + V_y + iV_x - iU_y) + \tfrac{1}{2}\mathcal{U}^*(U_x - V_y + iV_x + iU_y)$$

$$= (U + iV)_{\xi^*} \mathsf{L}\mathcal{A}^* e^{-if_0 t} + NRT, \tag{2.22}$$

16

We will denote $(U + iV)_{\xi^*}$ by $\frac{1}{2}\Upsilon$. Ignoring the NRT, the amplitude equation (2.12) then becomes:

$$\mathsf{L}\mathcal{A}_t + \mathrm{i}\beta y \mathsf{L}\mathcal{A} + \tfrac{1}{2}\mathrm{i}f_0\nabla_H^2\mathcal{A} + \mu_H(-\nabla_H^2)^n\mathsf{L}\mathcal{A} + \mu_V(-\partial_{zz})^n\mathsf{L}\mathcal{A} + \tfrac{1}{2}\Upsilon\mathsf{L}\mathcal{A}^* = 0. \quad (2.23)$$

2.1.1 The pumpwave train

As in Young *et al*, we will consider a pumpwave that is periodic in the horizontal directions with horizontal wave numbers (k, l), and frequency $\omega = 2f_0 + 2\sigma$, where $2\sigma \ll 2f_0$ is defined as the de-tuning frequency. Assuming that the pressure field associated with the pumpwave is given by:

$$P = a\cos(kx + ly - \omega t)\mathsf{p}_1(z) \quad (2.24)$$

where $\mathsf{p}_1(z)$ is the eigenfunction of the first vertical mode. We can then retrieve the corresponding horizontal velocities through the linear Boussinesq equations. Defining $\phi = kx + ly - \omega t$, we have:

$$U = \left[\frac{ak\omega}{\omega^2 - f_0^2}\cos\phi - \frac{alf_0}{\omega^2 - f_0^2}\sin\phi\right]\mathsf{p}_1(z), \quad (2.25)$$

$$V = \left[\frac{al\omega}{\omega^2 - f_0^2}\cos\phi + \frac{akf_0}{\omega^2 - f_0^2}\sin\phi\right]\mathsf{p}_1(z), \quad (2.26)$$

Plugging U and V into the definition of Υ, and retaining only the parts that results in resonance:

$$\Upsilon = 2(U + iV)_{\xi^*} = \frac{ia(k + il)^2}{2(\omega - f_0)}e^{i(kx + ly - 2\sigma t)}\mathsf{p}_1(z). \quad (2.27)$$

We can ignore the argument of $(k + il)^2$ since it just represents a constant phase shift of a. Defining

$$\upsilon = \frac{a(k^2 + l^2)}{2(\omega - f_0)} \approx \frac{a(k^2 + l^2)}{2f_0} \quad (2.28)$$

17

as the amplitude of the pumpwave, we have:

$$\Upsilon = \mathrm{i}\upsilon e^{\mathrm{i}(kx+ly-\omega t)}\mathsf{p}_1(z)\,. \tag{2.29}$$

In the numerical model of MacKinnon & Winters (2005), the ocean was assumed to be linearly stratified and have a constant buoyancy frequency: $N(z) = N_0$. In this case the first vertical mode will be:

$$\mathsf{p}_1(z) = \cos\left(\frac{\pi}{H}z\right)\,, \tag{2.30}$$

where H is the depth of the ocean. The dispersion relationship for internal gravity waves then results in a constraint on the horizontal wavenumbers k and l:

$$k^2 + l^2 = \frac{\omega^2 - f_0^2}{N_0^2 - \omega^2}\frac{\pi^2}{H^2} \approx \frac{3\pi^2 f_0^2}{N_0^2 H^2}\,, \tag{2.31}$$

where the buoyancy frequency N_0 is assumed to be much larger than f_0.

2.1.2 The simplified amplitude equation

We now look for solutions of the form

$$\mathcal{A} \approx \cos(mz)\,e^{-\mathrm{i}\sigma t}\left[e^{\mathrm{i}k_1 x}A_1(y,t) + e^{\mathrm{i}k_2 x}A_2^*(y,t)\right]\,, \tag{2.32}$$

where m is the local vertical wave number, and the horizontal wave numbers satisfy the resonant condition:

$$k_1 + k_2 = k\,. \tag{2.33}$$

If we assume that the vertical scale of the instabilities, m^{-1}, is small compared to scale over which the buoyancy frequency and the vertical structure of the pump wave vary, N and $\mathsf{p}_1(z)$ will be approximately constant. Taking $N(z)$ to be some characteristic frequency N_0 and $\mathsf{p} = 1$, we can introduce the scaled vertical wavenumber

$$\tilde{m} \equiv \frac{f_0 m}{N_0}\,, \tag{2.34}$$

18

and the differential operator L becomes:

$$\mathsf{L}\mathcal{A} = -\tilde{m}^2\mathcal{A}, \tag{2.35}$$

Substituting (2.29) and (2.32) into the amplitude equation (2.23) and separating the two harmonic components, we obtain a pair of coupled partial differential equations for the amplitudes $A_j(y,t)$. With the horizontal length scale (λ) and time scale (τ) defined as

$$\lambda = \left(\frac{f_0}{2\tilde{m}^2\beta}\right)^{1/3}, \quad \tau = \frac{1}{\lambda\beta}, \tag{2.36}$$

the non-dimensionalized equations are:

$$iA_{1\tilde{t}} = -A_{1\tilde{y}\tilde{y}} + \left(\tilde{y} - \tilde{b} - \tilde{a} - \tilde{\sigma}\right)A_1 + \tilde{v}e^{i\tilde{l}\tilde{y}}A_2^* - i\tilde{\mu}_H\left[\kappa_1 A_1 + (-1)^n A_{1\tilde{y}^{2n}}\right], \tag{2.37}$$

$$-iA_{2\tilde{t}} = -A_{2\tilde{y}\tilde{y}} + \left(\tilde{y} - \tilde{b} + \tilde{a} - \tilde{\sigma}\right)A_2 + \tilde{v}e^{-i\tilde{l}\tilde{y}}A_1^* + i\tilde{\mu}_H\left[\kappa_2 A_2 + (-1)^n A_{2\tilde{y}^{2n}}\right]. \tag{2.38}$$

In the above equations, the $\tilde{t} = \lambda\beta t$ and $\tilde{y} = y/\lambda$ are the non-dimensionalize independent variables, and $\tilde{k}_j = \lambda k_j$ and $\tilde{l} = \lambda l$ are the non-dimensionalized wave numbers. The non-dimensionalized pump wave amplitude $\tilde{v}$, de-tuning frequency $\tilde{\sigma}$ and dissipation parameter $\tilde{\mu}$ are given by:

$$\tilde{v} = \frac{v}{2\beta\lambda}, \quad \tilde{\sigma} = \frac{\sigma}{\beta\lambda}, \quad \tilde{\mu} = \frac{\mu_H}{\lambda^{2n+1}\beta}. \tag{2.39}$$

The parameters $\tilde{a}$ and $\tilde{b}$ are defined as:

$$\tilde{a} = -\frac{\lambda^2(k_1^2 - k_2^2)}{2}, \quad \tilde{b} = -\frac{\lambda^2(k_1^2 + k_2^2)}{2}. \tag{2.40}$$

The effective wave number is defined by:

$$\kappa_i = \tilde{k}_i^{2n}\left(1 + \frac{\mu_V m^{2n}}{\mu_H k_i^{2n}}\right) \tag{2.41}$$

19

(2.37) and (2.38) can be further simplified by removing some parameters, as their effects on the system can be understood easily. For example $\tilde{b} + \tilde{\sigma}$ can be removed via a shift in spatial coordinates $\tilde{y} - \tilde{b} - \tilde{\sigma} \to \tilde{y}$ together with a suitable constant phase shift in $A_{1,2}$, and therefore the effect of these two parameters is limit to a shift of the origin. If we assume that $k_1 = k_2$, the dissipative term $-i\tilde{\mu}_U\kappa_i$ can also be removed by a change of variable: $A_i \to e^{-\tilde{\mu}_H\kappa_i t}A_i$; this suggests that the effect of dissipation in the zonal and vertical direction is to suppress the amplitude of the PSI waves without altering the meridional structure, and hence we can ignore it. Finally we can also remove the parameter $\tilde{a}$ via $(A_1, A_2) \to \left(e^{i\tilde{a}t}A_1, e^{-i\tilde{a}t}A_2\right)$, and therefore the effect of $\tilde{a}$ is limited to a frequency shift.

With the above simplifications, as well as dropping the tildes, we have:

$$iA_{1t} = -A_{1yy} + yA_1 + ve^{ily}A_2^* - i\mu_H(-1)^n\partial_y^{2n}A1, \qquad (2.42)$$

$$-iA_{2t} = -A_{2yy} + yA_2 + ve^{-ily}A_1 + i\mu_H(-1)^n\partial_y^{2n}A_2. \qquad (2.43)$$

(2.42) and (2.43) will serve as the basis for the rest of this study.

2.2   Parameter estimation

We will close this chapter by providing a summary of the oceanographically relevant values for the physical parameters used in our scaling. In table 2.1, the pump wavenumber l and amplitude v are similar to the ones used in YTB. The buoyancy frequency of 0.0087s^{-1} is a value that is typically found in regions just underneath the mixed layer. These values, together with a vertical wave number of 100m, give a time scale of 30.5 days and a length scale of 19km; this length scale corresponds to a change of $0.171°$ in latitude.

M_2 tidal frequency	$1.405 \times 10^{-4} \text{s}^{-1}$
Coriolis frequency, $f_0 = \frac{1}{2}M_2$	$7.02 \times 10^{-5} \text{s}^{-1}$
Planetary vorticity gradient, β	$2.003 \times 10^{-11} \text{ m}^{-1} \text{ s}^{-1}$
Buoyancy frequency, N_0	$2\pi/720\text{s} = 0.0087\text{s}^{-1}$
Vertical wavenumber, m	$2\pi/100\text{m}$
Pump wavenumber, l	$2\pi/125\text{km}$
Pump amplitude υ	$1/5\text{days}$
Length scale, $\lambda = (f_0 N_0^2 / 2 f_0^2 m^2 \beta)^{1/3}$	19km
Time scale, $1/\beta\lambda$	30.5 days
Eddy viscosity scale, $\lambda^3\beta$	$1.36 \times 10^2 \text{m}^2\text{s}^{-1}$
Non-dimensional pump amplitude, $\hat{\upsilon} = \upsilon/(2\beta\lambda)$	3.04
nondimesnional pump wavenumber, $\hat{l} = \lambda l$	0.946

Table 2.1: Parameter values

Chapter 3

Dissipative Problem

In this chapter we will explore the solutions to the PDEs (2.42) and (2.43) derived in the previous chapter. We will mostly focus on the regular eddy dissipation model by taking $n = 1$, which results in

$$iA_{1t} = -(1 - i\mu)A_{1yy} + yA_1 + ve^{ily}A_2, \tag{3.1}$$

$$-iA_{2t} = -(1 + i\mu)A_{2yy} + yA_2 + ve^{-ily}A_1. \tag{3.2}$$

A set of energy equations can be derived for (3.1) and (3.2). The total energy density E can be defined as:

$$E \equiv \tfrac{1}{2}(u^2 + v^2) = \tfrac{1}{2}|\mathsf{L}\mathcal{A}|^2. \tag{3.3}$$

E is proportional to $|A_1|^2 + |A_2|^2$, and thus $E_n = |A_n|^2$ for $n = 1$, 2 can be interpreted as energy density for our equations. From (3.1) and (3.2), we can derive the following energy equations:

$$E_{1t} + J_{1y} = -D_1 + S, \tag{3.4}$$

$$E_{2t} + J_{2y} = -D_2 + S, . \tag{3.5}$$

with the meridional energy flux defined as

$$J_n(y,t) \equiv i(-1)^n \left(A_n^* A_{ny} - A_n A_{ny}^* \right) - \mu_H \left(A_{ny} A_n^* + A_{ny}^* A_n \right) . \tag{3.6}$$

The energy loss due to dissipation is given by

$$D_n(y,t) \equiv 2\mu_H |A_{ny}^2| , \tag{3.7}$$

and finally the energy source due to PSI is:

$$S = -iv \left(e^{ily} A_2 A_1^* - e^{-ily} A_2^* A_1 \right) . \tag{3.8}$$

3.1 An initial value problem

The controlling parameters in (3.1) and (3.2) are the dissipation (μ_H), the amplitude of the pumpwave/forcing (v), and the meridional wave number of the pumpwave (l). In the absence of the pumpwave and effect of dissipation, the equations reduce to the Schrödinger equation with a linear potential, which describes a particle falling under the influence of gravity. This is can be explained via a slowly varying wave approximation. Assuming that μ_H and v are small (and thus can be ignored), the A_1 equation takes the form:

$$iA_{1t} = -A_{1yy} + yA_1 \tag{3.9}$$

For the slowly varying wave approximation, we will assume $A_1 = e^{i\phi}$, where $\phi = \phi(y,t)$ is the phase. Defining the frequency $\hat{\omega} = -\phi_t$ and wave number $\hat{k} = \phi_y$, the dispersion relation for (3.9) is

$$\hat{\omega} = \hat{k}^2 + y. \tag{3.10}$$

Differentiating (3.10) with respect to y, and noting that $\hat{\omega}_y = -\phi_{ty} = -\hat{k}_t$, we now have a PDE for $\hat{k}$:

$$\hat{k}_t + 2\hat{k}\hat{k}_y = -1, \tag{3.11}$$

23

which can be solved using the method of characteristics. The solution is given by $\hat{k} = -t + \hat{k}_0$ on the characteristic curves $y - y_0 = -t^2 + 2\hat{k}_0 t$, where $\hat{k}_0$ and y_0 are respectively the initial wave number and position of the wave packet. The form of the characteristic curves suggest that the wave packet will indeed follow a ballistic trajectory, with the wave-packet having velocity $dy/dt = 2k = 2(t - \hat{k}_0)$; this suggest that for $t > \hat{k}_0$ the wave-packet will have negative velocity, and will be moving south. Eliminating t from the solution results in:

$$\hat{k}^2 = \hat{k}_0^2 + (y_0 - y), \tag{3.12}$$

which indicates that the wave number increases as the wave-packet travels south.

With the above observations, we can now formulate an initial value problem for PSI. Consider a perturbation in the near-inertial wave field in the form of a Gaussian wave packet with wave-number $k_0 > 0$ and :

$$A_1(y, 0) = e^{-(y-y_0)^2/\sigma} \cos(k_0 y) = \frac{1}{2} \left(e^{(y-y_0)^2/\sigma} e^{ik_0 y} + e^{(y-y_0)^2 sigma} e^{-ik_0 y} \right) \tag{3.13}$$

According to the analysis above, we expect the perturbation to split into two wave packets. The component with $e^{-ik_0 y}$ travels south, while the component with $e^{ik_0 y}$ will first travel north up to $y = k_0^2 + y_0$ before turning south. In the presence of the pump-wave (i.e. $v > 0$), the near-inertial wave-packets will grow due to PSI, and we would like to understand how the growth depends on the parameters.

3.1.1 Numerical scheme

As with other wave-type problems on an infinite domain, We will demand that the amplitude of the near-intertial waves decay to 0 as $y \to \pm\infty$; however there are some practical issues with truncating the problem to a finite domain $[y_L, y_R]$ for the numerical calculations as the boundary conditions (BC) at infinity are now applied

24

on a finite interval. For the right boundary y_R, the wave packet will be reflected before it reaches y_R provided that the initial kinetic energy is not too high, and thus we can simply set $A_1(y_R, t) = A_2(y_R, t) = 0$.

The situation at the left boundary y_L is complicated by the presence of $-A_{iyy} + yA_i$ in (3.1) and (3.2); the slowly varying wave theory predicts that the wave number increases as $\sqrt{|y|}$ as $y \to -\infty$ (see (3.12)). This presents us with a dilemma: on one hand the domain needs to be large in order for the wave amplitude to decay sufficiently to justify imposing a zero Dirichlet condition, but as the domain is extended by moving y_R towards $-\infty$ the grid needs to be refined to resolve the increasingly rapid oscillations.

One way to resolve this issue is to impose an absorbing boundary condition (ABC) in conjunction with truncation of the domain. There are two main types of ABCs: PDE-based and material based (for a brief review, see Zheng (2007)). PDE-based ABC relies on the ability to factor the differential operator, which in turn can be used to derive a radiative boundary condition that only allows out-going waves at the boundary. On the other hand, the material based ABC incorporates a sponge-like layer near the endpoint to absorbed outgoing waves. One class of material based ABC is the perfectly matched layer (PML), which was used by Berenger (1994) for the study of Maxwell's equations in electro-magnetics. It was also used sucessfully in both linear and non-linear Schrödinger's equation with variable potentials (Zheng, 2007).

As it is not clear how our equations can be factored to derive a radiative BC on the boundary, we will adopt the PML technique as outlined in Zheng (2007) for this numerical study. The main idea behind the method is to extend the computational domain from $[y_L, y_R]$ to $[y_{LR}, y_R]$ with $y_{LR} < y_L$. The PDE with the PML

is identical to the original PDE in the original domain of interest, while the PDE is modified in the sponge layer $[y_{LR}, y_L]$ by introducing an additional dissipative term that strongly damps out-going waves. The solutions are expected to decay exponentially, and hence a zero Dirichlet BC can be imposed at $y = y_{LR}$.

The primary function of the sponge layer is to ensure that the initial perturbation is not reflected back into the boundary, and thus allowing us to consider cases where the dissipation is too small to damp out the perturbations before it reaches the boundary. With the introduction of a PML, the second derivatives are modified via:

$$A_{1yy} \rightarrow -\frac{1}{1 - i\,\zeta(y)} \frac{\mathrm{d}}{\mathrm{d}y} \left(\frac{1}{1 - i\,\zeta(y)} A_{1y} \right) \tag{3.14}$$

$$A_{2yy} \rightarrow -\frac{1}{1 + i\,\zeta(y)} \frac{\mathrm{d}}{\mathrm{d}y} \left(\frac{1}{1 + i\,\zeta(y)} A_{2y} \right). \tag{3.15}$$

The absorption function $\zeta(y)$ is chosen to be:

$$\zeta(y) = \begin{cases} \zeta_0(y - y_l)^4 & \text{if } y_{LR} < y < y_L \\ 0 & \text{if } y_L \leq y < y_R \end{cases} \tag{3.16}$$

Equations (3.1) and (3.2) together with the initial condition

$$A_1(y, 0) = e^{-(y+25)^2/5} \cos(\sqrt{26}y), \quad A_2(y, 0) = 0 \tag{3.17}$$

are solved using a Crank-Nicolson finite difference scheme, which has the advantage of being unconditionally stable (Garcia, 1999).

We will now present a sample solution, where the computational grid is uniform both in space and time, with time-step $\Delta t = 0.00005$ and 4000 spatial grid-points over $[-100, 50]$. A sponge layer is located at $[-100, 85]$ with the $\zeta_0 = 0.01$. The amplitudes of the near-inertial wave field, $|A_1|$ and $|A_2|$, are shown in Figure 3.1. We can see that the wave packet splits up into two components that travel in

26

opposite directions. The northward propagating packet follows a ballistic trajectory while spreading out. At the same time we can see that as the wave packet moves through the domain it excites a standing wave that grows in amplitude over time. The standing wave is concentrated near the origin (the critical latitude), and the amplitude rapidly drops off to the south. This is not surprising as the effect of dissipation will be more potent as the wave-number increases to the south.
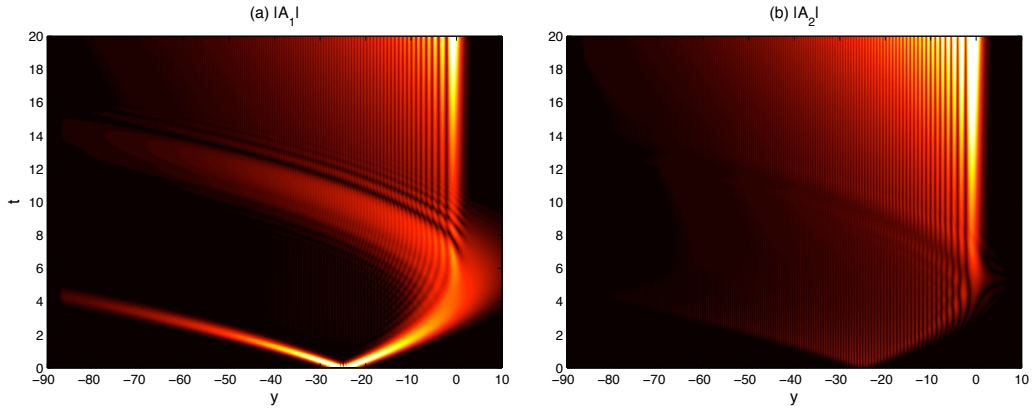

Figure 3.1: The results from a numerical computation of the PSI model. $|A_1|$ and $|A_2|$ are plotted in panels (a) and (b) respectively. The parameters used are $\upsilon = 0.25$, $l = 0$, and $\mu_H = 0.01$, with the spatial domain being $[-85, 50]$ and a sponge layer located at $[-100, -85]$. Only the data from $[-90, 10]$ is shown here.

3.2   Normal modes

The standing wave solutions can be best understood via an analysis of normal modes. The standing wave solution in the IVP decays exponentially to the south of the origin, and therefore we do not need to include a sponge layer in our problem. The domain can be truncated at a point sufficiently far south, and a zero Dirichlet boundary condition can be imposed. Assuming $A_n = A_n e^{\gamma t}$, where $\gamma = \gamma_R + i\gamma_I$,

(3.1) and (3.2) become:

$$(1 - i\mu)A_{1yy} = (y - i\gamma)A_1 + ve^{ily}A_2, \tag{3.18}$$

$$(1 + i\mu)A_{2yy} = (y + i\gamma)A_2 + ve^{-ily}A_1. \tag{3.19}$$

This system is now an eigenvalue problem, and the boundary conditions are the same as the PDE: $|A_n| \to 0$ as $y \to \pm\infty$.

3.2.1 Numerical solution

To investigate the effect of the three parameters v, l, and μ on the eigenvalues, we will compute the eigenvalues numerically. The second derivatives in (3.18) and (3.19) are discretized using a centered final difference scheme, and the eigenvalue problem becomes a matrix eigenvalue problem; the matrix is large but sparse, which can be handled via the `eigs` function in MATLAB. `eigs` is an iterative numerical scheme that estimates the eigenvalues for matrices, and it is useful when only part of the spectra is of interest.

We will compute the spectra over $[y_L, 50]$ for some y_L, and impose zero Dirichlet boundary condition at both end-points. We will then take the limit as $y_L \to -\infty$; if the eigenvalues converge to a limit, the limit can be interpreted as the eigenvalues of the problem over the infinite interval. We found that the eigenvalues and eigenfunctions only differ slightly with the zero Dirichlet BC is replaced by a sponge layer at the southern boundary, and therefore we will ignore the sponge layer in this section.

Zonally propagating pump-wave: $l = 0$

Figure 3.2 shows the result for a series of calculations with $v = 1$, and $l = 0$. The eigenvalue problem is solved over a domain of $[-100, 50]$, and the real part of the

normalized eigenfunctions $\Re(A_1)$ over $[-60, 10]$ are plotted on the left column of figure 3.2. $\mu = 1$, 10^{-1}, 10^{-2}, 10^{-4}, and 0 were used in the calculations; the plots are arranged in decreasing order of μ from top to bottom. One can see that in all cases, the eigenfuction is oscillatory to the south (when $y < 0$), while to the north of the turning point $y = 0$, the eigenfunction quickly decays to 0, indicating that the near-inertial waves are evanescent as expected. On the bottom row, the numerically computed eigenfunction (blue curve) is almost indistinguishable from the Airy function (red curve) in the absence of dissipation; in §3.2.2 we will show that the Airy function is the exact solution to the inviscid problem. When dissipation is increased to 10^{-4}, the eigenfunction still resembles the airy function, but the amplitude to the south is significantly reduced. As dissipation is increased further, the wave becomes more and more localized to the turning latitude.

The spectra for each case is plotted on the right column. In the inviscid limit $\mu = 0$ (bottom panel) the eigenvalues are either purely real (growing or decaying modes), or purely imaginary (neutral modes). The fastest growing mode has a growth rate close to 1. As the dissipation increases, to $\mu = 10^{-2}$, the majority of the modes become decaying, with a handful of modes that remain unstable. When the dissipation is further increased to 1, all but one of the modes become stable, and the growth rate of the unstable mode is now significantly lower then the inviscid case. The eigenvalues becomes insensitive to y_L for $y_L < -100$, and therefore the computed spectra should be a good approximation to the spectra on the infinite interval.
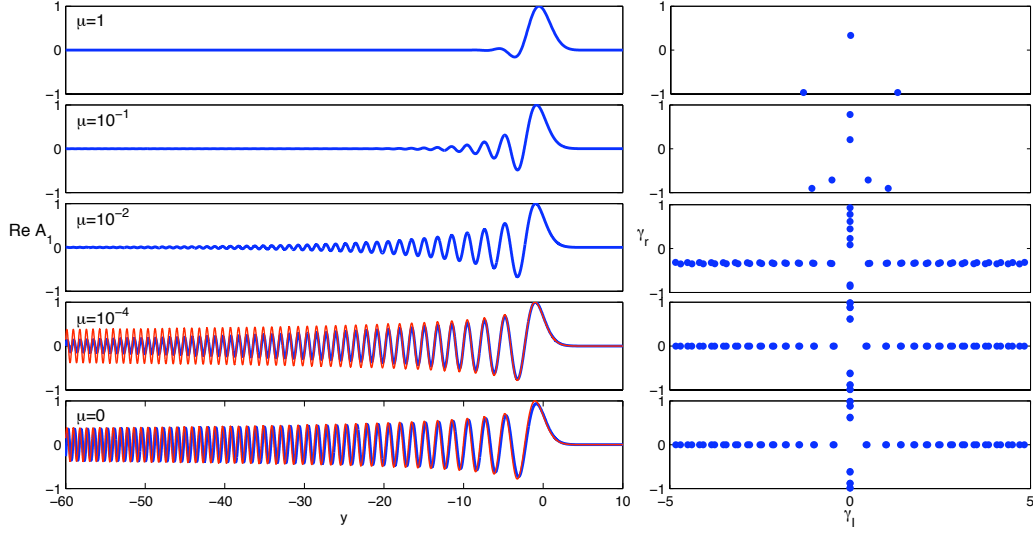
29

Figure 3.2: *Effect of dissipation on the spectrum:* $l = 0$: The dissipation parameter used (from top to bottom) are $\mu = 1$, 10^{-1}, 10^{-2}, 10^{-4}, and 0. On the left column the real part of the eigenfuctions associated with the fastest growing modes are plotted in blue, while in the last two panel the airy function $\mathrm{Ai}(y)$ is also plotted in red. On the right column the spectra are plotted, with the abiscissa and ordinate being respectively the imaginary part and the real part (the growth rate) of the eigenvalues. $v = 0$ for all calculations.

More general case: $l \neq 0$

We will now turn to the case where l is no longer zero. In figure 3.3, the results from a set of computations with $v = 1$ and $l = 0.1$ is shown, with $\mu = 1$, 10^{-1}, 10^{-2}, 10^{-3}, 10^{-4}, and 0. The computations are repeated over the domain $[y_L,\, 20]$, where y_L was varied to determine the effect of truncation. The results with $y_L = -100$ are plotted in blue, while the results with $y_L = -150$ are plotted in red. Notice that only parts of the eigenfunctions over $[-80,\, 10]$ are shown, and the scale for the frequency of the spectra plot is different from figure3.2.

For large values of dissipation (top two rows in figure 3.3), the results from both values of y_L agree, showing that neither the eigenfunction nor the physically
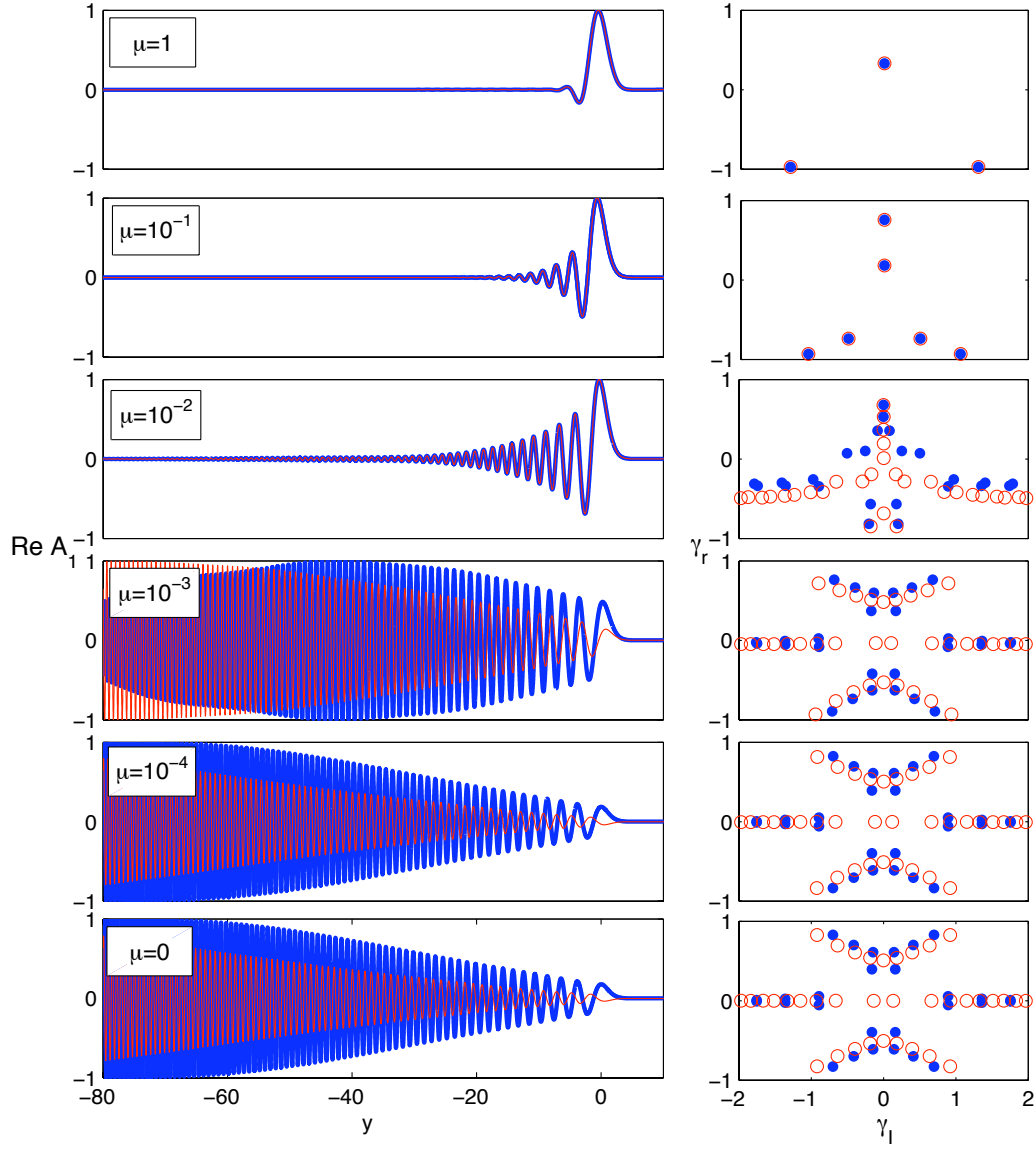
Figure 3.3: *Effect of dissipation on the spectrum:* $l = 0.1$: The dissipation parameter used (from top to bottom) are $\mu = 1, 10^{-1}, 10^{-2}, 10^{-3}, 10^{-4}$, and 0. On the left column the real part of the eigenfuctions associated with the fastest growing modes are plotted; in blue are the results from using a domain of $[-100, 20]$, while the curves in red are based on a domain of $[-150, 20]$. The corresponding spectra are respectively plotted with blue dots and red circes. The abiscissa and ordinate are respectively the imaginary part and the real part (the growth rate) of the eigenvalues. $\upsilon = 1$ for all calculations

interesting portion of the spectra is affected by the change in y_L. As in the $l = 0$ case, the eigenfunction decays quickly to zero due to dissipation, and there are a small number of discrete unstable modes. When dissipation is decreased to 10^{-2}, the two computations agree for the fastest growing mode, but the spectra plot reveals that the domain length starts to affect the computation. The computation with $y_L = -100$ suggests the presence of unstable modes that have non-zero frequency (i.e. $\gamma_I \neq 0$), while the computation with $y_L = -150$ suggests that all unstable modes have zero frequency.

As the dissipation is decreased further (bottom three rows), the picture is very different from the $l = 0$ case. The spectra plots show that most unstable modes now have non-zero frequency, and the frequency increases as the $y_L \to \infty$. The plots of the eigenfunction reveal that the waves are no longer localized to the turning latitude; instead, the bulk of the wave is located at the center of the domain, and moves as the boundary moves southwards. We will refer these modes as 'boundary modes'.

To get a better understanding of the transition between the boundary and localized modes as μ changes, we performed a series of computations where y_L and μ were varied systematically: the boundary was moved from $y_L = -80$ to $y_L = -200$, and for each series μ was varied from 10^{-4} to 1, with $\upsilon = 1$ and $l = 0.1$. The results are presented in figure 3.4, where the frequency (γ_I) and growth rate (γ_R) of the most unstable mode are plotted as a function of dissipation. When the dissipation is small ($\mu \approx 10^{-3}$), the growth rate (bottom panel) depends on y_L, but the sensitivity is reduced as dissipation vanishes; the graph suggests that as we approach the inviscid limit, the growth rate will converge to a value that is independent of y_L; however, while the frequency (top panel) is insensitive to dissipation, the frequency remains
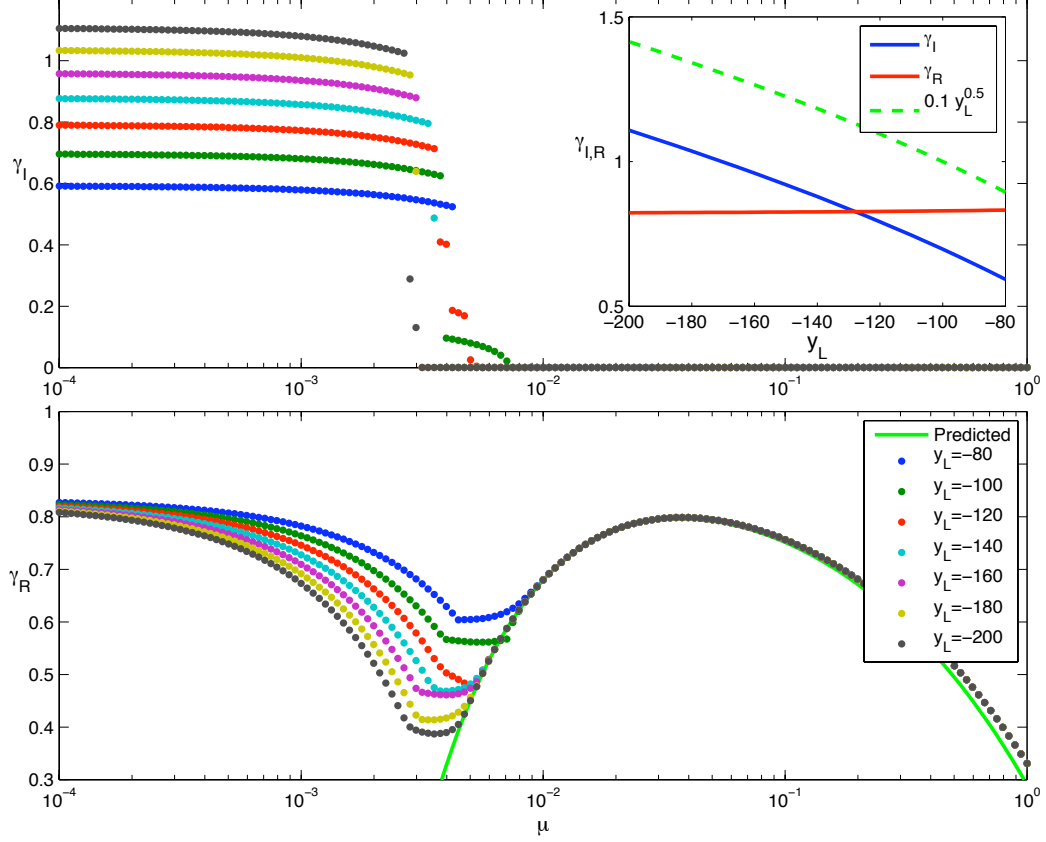
Figure 3.4: *Effect of computational domain on the eigenvalues.* The frequency (γ_I, top panel) and growth rate (γ_R, bottom panel) of the most unstable modes are plotted as a function of μ on a semi-log scale. The computation domain $[y_L, 20]$ ranges from $y_L = -80$ to $y_L = -200$, and the results from each series are marked by dots. The predicted growth rate from (3.74) is also plotted in the bottom panel as the green curve. *Inset:* γ_R and γ_I as a function of y_l in the inviscid limit. $\upsilon = 1$ and $l = 0.1$ for all calculations.

dependent on y_L. The effect of y_L on the eigenvalues for the inviscid problem ($\mu = 0$) is shown in the inset of figure 3.4. The growth rate depends very weakly on y_L, but the frequency increases approximately as $l\sqrt{y_L}$ (plotted as the green dashed line). The eigenfunctions for the unstable modes in the inviscid problem resemble the boundary modes plotted in the bottom panel of figure 3.3.
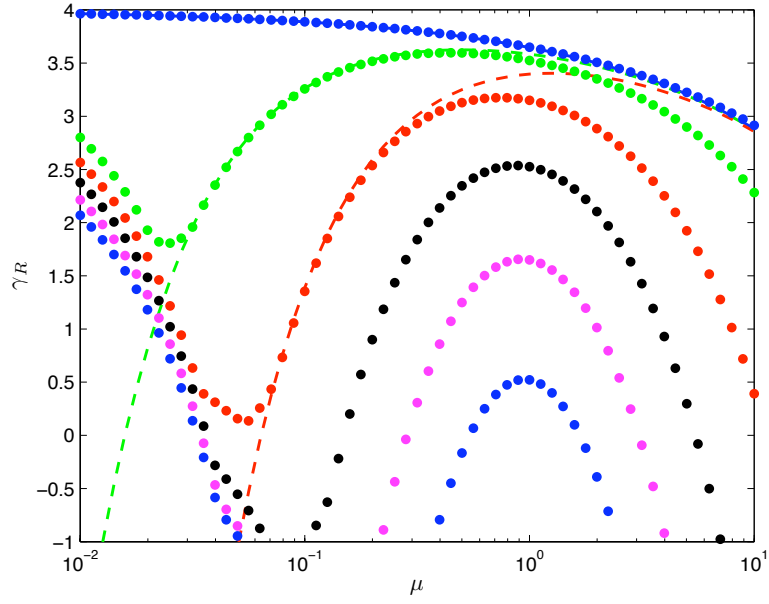
A question regarding these boundary modes is whether they are artifacts resulting from grid instabilities, but this can be discounted since the rapid oscillations in the eigenfunctions are well resolved, and a change in grid size does not affect the result. It is also not due to the zero Dirichlet boundary condition imposed at the southern boundary, as the eigenvalues and eigenfunction of the boundary modes are only affected minimally if the zero Dirichlet BC is replaced by a sponge layer or a radiative (Sommerfeld) type boundary condition that eliminates incoming waves at the boundary. Since the frequency of the boundary mode does not appear to converge, and the location of peak of the eigenfunctions changes as the y_L is moved to the south, the conclusion is that these modes are un-physical.

We will now return to figure 3.4. From the inviscid limit, the growth rate of these boundary modes rapidly decreases as dissipation is increased, with the mode from $y_L = -200$ being most susceptible to dissipation. There is a sudden break in the graph when μ inceases to $10^{-2.5}$, and the numerically computed growth rates now converge to a single curve, and no longer depends on y_L. The frequency also undergoes a similar transition: as the frequency increases pass the transition near $\mu \approx 10^{-2.5}$, all the curves collapse to abruptly to 0. This marks the transition from the boundary modes to modes where both the eigenvalues and eigenfunctions are independent of the location of the boundary. These new modes are physically meaningful since the choice of the locaion of the boundary does not affect the structure
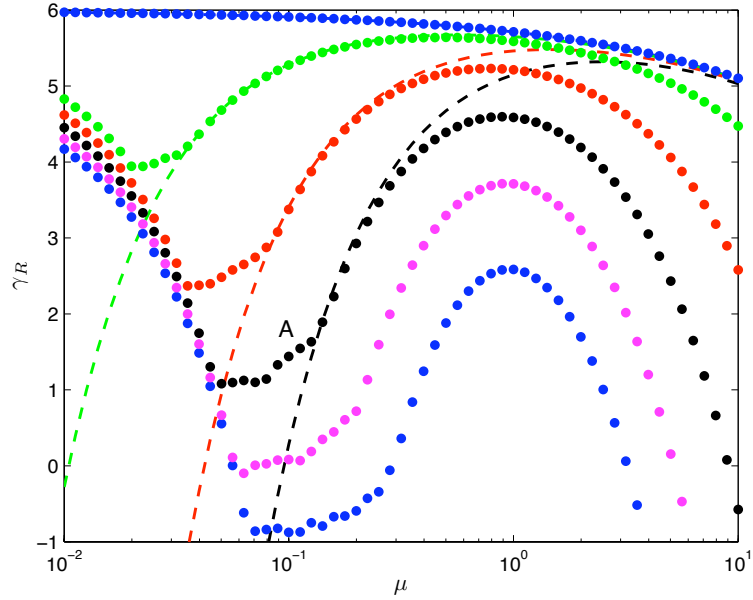
or growth rate of the mode. The eigenfunctions are similar to the localized modes in the top three panels of figure 3.3.

A curious feature is that the effect of dissipation on these localized modes is not monotonic: while an increase in dissipation for larger values of μ stabilizes the system, the growth rate in fact increases with μ when dissipation is small (between $10^{-2.5}$ to $10^{-1.7}$); this result rather surprising, as one would normally expect dissipation to have a stabilizing effect. We will explore this behaviour via the energy equations in §3.2.3.

We will now present a couple of plots in figure 3.5, which summarize the effect of the various parameters on the growth rate for $\upsilon = 4$ (top panel) and $\upsilon = 6$ (bottom panel). The two plots are qualitatively similar. For $l = 0$ (top series), $\gamma_R \approx \upsilon$ when the dissipation is small, and decreases monotonically as μ increases. For $l \neq 0$, the non-monotonic effect of dissipation on growth rate observed earlier holds for a wide range of l. An increase in l reduces the growth rate, and for sufficiently large value of l, the normal modes become stable for small μ. For example, when $l = 2.5$ and $\upsilon = 4$ (bottom series in the top panel of figure 3.5), the growth rate is negative for $\mu < 10^{-0.5}$.

(a) $v = 4$

(b) $v = 6$

Figure 3.5: *Effect of the parameters on the growth rate.* The growth rates are plotted as a function of μ for different values of pump wavenumber l (dots); from top to bottom, $l = 0$, 0.5, 1,1.5, 2, and 2.5. The dashed lines are the growth waves predicted by the short wave theory in §3.2.2(c.f. (3.74)). For all calculations, the eigenvalue problem was solve over the domain $[-100, 20]$.

3.2.2 Analytical results

We will now develop some analytical results which provides support to our numerically computed growth rates. The most important result is an analytical prediction for limit where $0 < l \ll 1$ and $\mu \ll 1$, as it confirms our numerical results showing that $\mu \to 0$ stabilizes the system for a non-zero l. The problem with $\mu = l = 0$ can be solvable exactly, which is then used as the basis of a perturbative solution with l and μ as a small parameter.

A zonally propagating pump-wave in the inviscid limit

We will first consider the inviscid limit ($\mu = 0$), as well as a pump-wave that propagates zonally ($l = 0$), as in this regime the eigenvalue problem can be diagonalized and solved exactly:

$$\begin{bmatrix} A_1(y) \\ A_2(y) \end{bmatrix} = \begin{bmatrix} \upsilon & -i\gamma - \sqrt{\upsilon^2 - \gamma^2} \\ i\gamma + \sqrt{\upsilon^2 - \gamma^2} & \upsilon \end{bmatrix} \begin{bmatrix} c_1 \mathrm{Ai}(y - \sqrt{\upsilon^2 - \gamma^2}) \\ c_2 \mathrm{Ai}(y + \sqrt{\upsilon^2 - \gamma^2}) \end{bmatrix} \tag{3.20}$$

The fundamental solutions are $\mathrm{Ai}(y \pm \sqrt{\upsilon^2 - \gamma^2})$, where $\mathrm{Ai}(y)$ is the Airy function of the first kind. The argument of $\mathrm{Ai}(y)$ must be real for $\mathrm{Ai}(y)$ to remain bounded as $y \to \pm\infty$, which implies that γ must be real and $\upsilon^2 - \gamma_R^2 \geq 0$. The latter condition implies that there is a continuous spectrum of normal modes, with growth rates satisfying the inequality:

$$-\upsilon \leq \gamma_R \leq \upsilon. \tag{3.21}$$

The maximum growth rate is $\gamma_{R\,max} = \upsilon$, which agrees with the numerically obtained growth rates (c.f. figure 3.5 and the bottom panel of figure 3.3). The eigenfunctions associated with the fastest growing mode are $A_1(y) = \mathrm{Ai}(y)$ and $A_2(y) = i\,\mathrm{Ai}(y)$. Using (3.6), It can be shown that the meridional energy flux is

identically 0. The interpretation is that the fastest growing near-inertial oscillations excited by a zonally propagating pump-wave will only transport energy zonally.

Young *et al.* (2008) found the growth rate for a zonally propagating pump-wave at the critical latitude $28.9°$ to be (with the variables non-dimensionalized as the present study):

$$\gamma_{Rmax} = \sqrt{v^2 - (b+\sigma)^2}\,, \tag{3.22}$$

Curiously the factor $b+\sigma$ in (3.22) is identical to the spatial shift we initially ignored in the IVP problem, yet it plays no role in the growth rate for our analysis. It is perhaps instructive to re-concile the two results.

Discarding the β-effect term yA_n, and re-inserting $b+\sigma$ into our equations, the eigenvalue problem becomes:

$$A_{1yy} = (-(b+\sigma) - i\gamma)\,A_1 + v\,A_2\,, \tag{3.23}$$

$$A_{2yy} = (-(b+\sigma) + i\gamma)\,A_2 + v\,A_1\,, \tag{3.24}$$

Since y does not explicitly appear in the equations, we can seek solutions that are periodic in y: $A_1 = e^{il_1 y}$ and $A_2 = e^{-il_2 y}$. To satisfy the resonant condition, the wave numbers must satisfy $l_1 + l_2 = 0$, and the eigenvalues are:

$$i\gamma = i\sqrt{v^2 - \left[l_1^2 - (b+\sigma)\right]^2}\,. \tag{3.25}$$

YTB considered the reduced 2-dimensional model in the absence of the $\beta-$effect, and seeked solutions that are uniform in y; this is equivalent to setting l_1 in (3.25) to be 0 and we will recover their result (3.22). On the other hand, there is no reason to restrict ourselves to meridionally uniform solutions, and thus (3.25) is a more general result for the model of YTB. This equation suggests that maximum growth rate $\gamma_{max} = v$ can be achieved when $l_1 = \sqrt{b+\sigma}$, and therefore there is scale selection in the y-direction at the critical latitude.

This scale selection behaviour is consistent with our model. If we retain $b + \sigma$ in our governing equations, the corresponding eigenfuction is $\text{Ai}(y - (b + \sigma))$ which has a turning point at $y = b + \sigma$; to the south of the turning point the Airy function is periodic with local wave-number $\sqrt{|y - (b + \sigma)|}$, while to the north the wave becomes evanescent. Now if $(b + \sigma) \gg 1$, then the critical latitude $y = 0$ lies to the south of the turning point; therefore the waves at the critical latitude will be periodic with wave-number $\sqrt{(b + \sigma)}$, which is consistent with the analysis in the preceding paragraph.

Short wave theory

We can use the analytical solution to the $\mu = l = 0$ problem in the previous section to make progress analytically for cases where the the parameters υ and l are non-zero but small. It is convenient to consider a change in variables:

$$f(y) = A_1 e^{-ily/2} - iA_2 e^{ily/2}, \quad ig(y) = A_1 e^{-ily/2} + iA_2 e^{ily/2} \tag{3.26}$$

Our equations then become:

$$f'' - lg' - \frac{l^2}{4}f + \mu g'' + \mu l f' - \mu \frac{l^2}{4}g - yf - (\upsilon + \gamma)g = 0, \tag{3.27}$$

$$g'' + lf' - \frac{l^2}{4}g - \mu f'' + \mu l g' + \mu \frac{l^2}{4}f - yg - (\upsilon - \gamma)f = 0. \tag{3.28}$$

In the previous section, the numerical results suggest that the unstable modes have frequency that vanishes ($\gamma_I = 0$), and therefore we will assume that γ, f and g in (3.27) and (3.28) are purely real. In addition we can easily verify that $f(y) = \text{Ai}(y)$, $g(y) = 0$, and $\lambda = \upsilon$ are solutions to the above system. With a small parameter defined as $\epsilon = \sqrt{\mu}$, as well as the assumption that l scales as $\epsilon^{3/2}$ (i.e. $l = l_{3/2}\epsilon^{3/2}$),

(3.27) and (3.28) becomes

$$f'' - l_{3/2}\epsilon^{3/2}g' + \epsilon^2 g'' - yf - (v + \gamma)g = O(\epsilon^{5/2}), \tag{3.29}$$

$$g'' + l_{3/2}\epsilon^{3/2}f' - \epsilon^2 f'' - yg - (v - \gamma)f = O(\epsilon^{5/2}). \tag{3.30}$$

Inner solution

We will seek an expansion of the form:

$$f = \text{Ai}(y) + \epsilon^{1/2}f_{1/2}(y) + \cdots, \tag{3.31}$$

$$g = \epsilon^{1/2}g_{1/2}(y) + \epsilon g_1(y) \cdots, \tag{3.32}$$

$$\gamma = v + \epsilon\gamma_1 + \cdots. \tag{3.33}$$

Plugging (3.31) to (3.33) into (3.29) and (3.30) and gathering the $O(\epsilon^{1/2})$ terms, we have:

$$f''_{1/2} - yf_{1/2} = 2vg_{1/2}, \tag{3.34}$$

$$g''_{1/2} - yg_{1/2} = 0. \tag{3.35}$$

(3.35) is satisfied by $g_{1/2} = r\text{Ai}(y)$, where r is a constant that is to be determined later. Since $(Ai')'' = (Ai'')' = (yAi)'$, a particular solution to (3.34) is

$$f_{1/2} = 2vr\text{Ai}'(y). \tag{3.36}$$

Moving on to $O(\epsilon)$ terms in (3.30), we have:

$$g''_1 - yg_1 = \gamma_1 Ai, \tag{3.37}$$

which has the particular solution:

$$g_1 = -\gamma_1 \text{Ai}'(y), \tag{3.38}$$

40

To summarize, the inner solution is:

$$f = \text{Ai}(y) + \epsilon^{1/2} 2 v r \text{Ai}'(y) + \cdots , \tag{3.39}$$

$$g = \epsilon^{1/2} r \text{Ai}(y) - \epsilon \gamma_1 \text{Ai}'(y) + \cdots , \tag{3.40}$$

The Outer Region

As $y \to -\infty$, standard asymptotic formulae for the Airy function give (Abramowitz & Stegun, 1964):

$$\text{Ai}(y) \sim \frac{1}{\sqrt{\pi} \sqrt[4]{-y}} \sin\left(\phi + \frac{\pi}{4}\right) \text{ and} \tag{3.41}$$

$$\text{Ai}'(y) \sim \frac{\sqrt[4]{-y}}{\sqrt{\pi}} \cos\left(\phi + \frac{\pi}{4}\right) , \tag{3.42}$$

where $\phi(y) = \frac{2}{3}|y|^{3/2}$ is the phase. Since the solution becomes increasingly oscillatory, we anticipate that some of the derivatives we neglected in the inner region may become important. In addition, (3.42) suggests that the $O(\epsilon)$ term in $g(y)$ grows as $y \to -\infty$, which leads to a break in the order. Both of these observations point to the existence of an outer solution which we will need to match onto the inner solution (which we will relabel as f_{in} and g_{in}) given by (3.39) and (3.40). To proceed we will define $Y = \epsilon y$ as the outer variable; notice that in terms of the outer variable,

$$f \sim \epsilon^{1/4} \left[\frac{1}{\sqrt[4]{-Y}} \sin\left(\frac{\phi(Y)}{\epsilon^{3/2}} + \frac{\pi}{4}\right) + 2 v r \sqrt[4]{-Y} \cos\left(\frac{\phi(Y)}{\epsilon^{3/2}} + \frac{\pi}{4}\right) \right] \text{ and} \tag{3.43}$$

$$g \sim \epsilon^{3/4} \left[\frac{r}{\sqrt[4]{-Y}} \sin\left(\frac{\phi(Y)}{\epsilon^{3/2}} + \frac{\pi}{4}\right) - \gamma_1 \sqrt[4]{-Y} \cos\left(\frac{\phi(Y)}{\epsilon^{3/2}} + \frac{\pi}{4}\right) \right] , \tag{3.44}$$

41

We have scaled the inner solutions to remove the constant factor of $1/\sqrt{\pi}$. Motivated by the form of the inner solution, we seek a WKBJ-type solution in the outer region:

$$f_{out} = \epsilon^{1/4} \left[R_1(Y) \sin\left(\frac{\phi(Y)}{\epsilon^{3/2}}\right) + R_2(Y) \cos\left(\frac{\phi(Y)}{\epsilon^{3/2}}\right) \right] \text{ and} \qquad (3.45)$$

$$g_{out} = \epsilon^{3/4} \left[S_1(Y) \sin\left(\frac{\phi(Y)}{\epsilon^{3/2}}\right) + S_2(Y) \cos\left(\frac{\phi(Y)}{\epsilon^{3/2}}\right) \right]. \qquad (3.46)$$

In terms of the outer variable, the scaled equations are:

$$\epsilon^2 \frac{d^2 f_{out}}{dY^2} - l_{3/2}\epsilon^{5/2}\frac{dg_{out}}{dY} + \epsilon^4 \frac{d^2 g_{out}}{dY^2} - \frac{Y}{\epsilon}f - (2\upsilon + \epsilon\gamma_1)g = O(\epsilon^{5/2}), \qquad (3.47)$$

$$\epsilon^2 \frac{d^2 g_{out}}{dY^2} + l_{3/2}\epsilon^{5/2}\frac{df_{out}}{dY} - \epsilon^4 \frac{d^2 f_{out}}{dY^2} - \frac{Y}{\epsilon}g + \epsilon\gamma_1 f = O(\epsilon^{5/2}), \qquad (3.48)$$

We will now proceed with the asymptotic expansion by substituting (3.45) and (3.46) into (3.47) and (3.48). The leading order equation gives:

$$\frac{d\phi}{dY} = \pm\sqrt{-Y} \qquad (3.49)$$

for both equations. We will take the negative root as its integral is consistent with the definition of the phase function $\phi(Y) = \frac{2}{3}|Y|^{3/2}$. At the next order, the equations contain both sine and cosine terms, and their coefficients must vanish for the equations to hold. We can therefore extract four equations:

$$2\frac{dR_1}{dY}\frac{d\phi}{dY} + R_1\frac{d^2\phi}{dY^2} = 2\upsilon S_2 \qquad (3.50)$$

$$2\frac{dR_2}{dY}\frac{d\phi}{dY} + R_2\frac{d^2\phi}{dY^2} = -2\upsilon S_1 \qquad (3.51)$$

$$2\frac{dS_1}{dY}\frac{d\phi}{dY} + S_1\frac{d^2\phi}{dY^2} = -\gamma_1 R_2 - l_{3/2}\frac{d\phi}{dY}R_1 - \frac{d\phi}{dY}^2 R_2 \qquad (3.52)$$

$$2\frac{dS_2}{dY}\frac{d\phi}{dY} + S_2\frac{d^2\phi}{dY^2} = +\gamma_1 R_1 - l_{3/2}\frac{d\phi}{dY}R_2 + \frac{d\phi}{dY}^2 R_1 \qquad (3.53)$$

These can be simplified by defining $\eta = \sqrt[4]{8\upsilon}\sqrt{-Y}$, and $\hat{R}_n, \hat{S}_n = R_n\sqrt{\eta}, S_n\sqrt{\eta}$.

With $\frac{d\phi}{dY} = -\sqrt{-Y} = -\eta/\sqrt[4]{8v}$, $\frac{d^2\phi}{dY^2} = \sqrt[4]{8v}/(2\eta)$, (3.50) to (3.53) simplifies to:

$$\hat{R}_{1\eta} = \frac{2v}{\sqrt[4]{8v}}\hat{S}_2 \tag{3.54}$$

$$\hat{R}_{2\eta} = -\frac{2v}{\sqrt[4]{8v}}\hat{S}_1 \tag{3.55}$$

$$\hat{S}_{1\eta} = \frac{1}{\sqrt[4]{8v}}\left[-\gamma_1 R_2 + \frac{\eta}{\sqrt[4]{8v}}l_{3/2}R_1 - \frac{\eta^2}{\sqrt{8v}}R_2\right] \tag{3.56}$$

$$\hat{S}_{2\eta} = \frac{1}{\sqrt[4]{8v}}\left[\gamma_1 R_1 + \frac{\eta}{\sqrt[4]{8v}}l_{3/2}R_2 + \frac{\eta^2}{\sqrt{8v}}R_1\right] \tag{3.57}$$

Eliminating $\hat{S}_1$ and $\hat{S}_2$ from (3.54) to (3.57), and defining $A = \gamma_1\sqrt{\frac{v}{2}}$ and $B = \frac{l_{3/2}}{2}\sqrt[4]{\frac{v}{2}}$, we have a pair of coupled second order ODE:

$$\hat{R}_{1\eta\eta} - \left(\frac{\eta^2}{4} + A\right)\hat{R}_1 = B\eta\hat{R}_2 \tag{3.58}$$

$$\hat{R}_{2\eta\eta} - \left(\frac{\eta^2}{4} + A\right)\hat{R}_2 = -B\eta\hat{R}_1 \tag{3.59}$$

It turns out that the pair can be uncoupled by defining $F_1 = \hat{R}_1 + i\hat{R}_2$ and $F_2 = \hat{R}_1 - i\hat{R}_2$, the differential equations for F_1 and F_2 are:

$$F_{1\eta\eta} - \left(\frac{1}{4}(\eta + 2iB)^2 + B^2 + A\right)F_1 = 0\,, \tag{3.60}$$

$$F_{2\eta\eta} - \left(\frac{1}{4}(\eta - 2iB)^2 + B^2 + A\right)F_2 = 0\,, \tag{3.61}$$

both of which have parabolic cylinder functions as solutions. For the outer solutions $f_{out}(Y)$ and $g_{out}(Y)$ we demand that they decay to zero as $Y \to -\infty$, which is equivalent to $|F_{1,2}| \to 0$ as $\eta \to \infty$. The standard solutions to the parabolic cylinder equations are given by $\mathcal{U}(a, x)$ and $\mathcal{V}(a, x)$, and only $\mathcal{U}(a, x)$ decays as $x \to \infty$ (Abramowitz & Stegun, 1964). Hence we have:

$$F_1(\eta) = c_1\mathcal{U}(B^2 + A, \eta + 2iB) \quad \text{and} \quad F_2(\eta) = c_2\mathcal{U}(B^2 + A, \eta - 2iB)\,, \tag{3.62}$$

where c_1 and c_2 are constants that are determined by matching with the inner solution.

Matching

To match up the inner and outer regions, the outer solution should take the form of (3.45) and (3.46) as $Y \to 0$. To facilitate matching, we will expand (3.45) and (3.46)

$$f_{in} \sim \epsilon^{1/4} \left[\left(\frac{1}{\sqrt[4]{-Y}} + 2vr\sqrt[4]{-Y} \right) \sin\left(\frac{\phi(Y)}{\epsilon^{3/2}} \right) + \left(\frac{1}{\sqrt[4]{-Y}} - 2vr\sqrt[4]{-Y} \right) \cos\left(\frac{\phi(Y)}{\epsilon^{3/2}} \right) \right],$$

(3.63)

$$g_{in} \sim \epsilon^{3/4} \left[\left(\frac{r}{\sqrt[4]{-Y}} + 2v\sqrt[4]{-Y} \right) \sin\left(\frac{\phi(Y)}{\epsilon^{3/2}} \right) + \left(\frac{r}{\sqrt[4]{-Y}} - 2v\sqrt[4]{-Y} \right) \cos\left(\frac{\phi(Y)}{\epsilon^{3/2}} \right) \right],$$

(3.64)

with the constant factors $\sqrt{2}/2$ being scaled out.

Comparing the f_{in} and f_{out} from (3.45), we will need the coefficients of the sine and cosine terms to match as $Y \to 0$. Remembering that $\hat{R}_n = R_n\sqrt{\eta}$ and $\sqrt{-Y} = \eta/\sqrt[4]{8v}$, it suggests that near $Y = 0$, the matching conditions are:

$$\hat{R}_1(\eta) \sim \sqrt[4]{8v} + 2vr\eta \quad \text{and} \quad \hat{R}_2(\eta) \sim \sqrt[4]{8v} - 2vr\eta,$$

$$\implies \hat{R}_1(0) = \hat{R}_2(0) = \sqrt[4]{8v} \quad \text{and} \quad \hat{R}'_1(0) = -\hat{R}'_2(0) = 2vr.$$

(3.65)

Similarly, comparing g_{in} and g_{out} gives

$$\hat{S}_1(\eta) \sim r\sqrt[4]{8v} - \gamma_1\eta \quad \text{and} \quad \hat{S}_2(\eta) \sim r\sqrt[4]{8v} + \gamma_1\eta.$$

$$\implies \hat{S}_1(0) = \hat{S}_2(0) = r\sqrt[4]{8v} \quad \text{and} \quad \hat{S}'_1(0) = -\hat{S}'_2(0) = -\gamma_1.$$

(3.66)

With the help of (3.54) to (3.57), we can see that the boundary conditions given by (3.66) are automatically satisfied as long as the boundary conditions in (3.65) are satisfied. The conditions $\hat{R}_1(0) = \hat{R}_2(0)$ and $\hat{R}'_1(0) = -\hat{R}'_2(0)$ from (3.65) in turn require that

$$F_1(0) = iF_2(0) \quad \text{and} \quad F'_1(0) = -iF'_2(0)$$

(3.67)

44

or equivalently,

$$
\begin{bmatrix} \mathcal{U}(B^2+A, 2iB) & -i\mathcal{U}(B^2+A, -2iB) \\ i\mathcal{U}'(B^2+A, 2iB) & -\mathcal{U}'(B^2+A, -2iB) \end{bmatrix} \begin{bmatrix} c_1 \\ c_2 \end{bmatrix} = \begin{bmatrix} 0 \\ 0 \end{bmatrix}, \tag{3.68}
$$

For the system (3.68) to have a non-trivial solution, the determinant of the matrix must vanish:

$$
\mathcal{U}(B^2+A, 2iB)\mathcal{U}'(B^2+A, -2iB) + \mathcal{U}(B^2+A, -2iB)\mathcal{U}'(B^2+A, 2iB) = 0. \tag{3.69}
$$

Now the Wronskian of $\mathcal{U}(a, x)$ and $\mathcal{U}(a, -x)$ is given by

$$
(\mathcal{U}(a, x))'\, \mathcal{U}(a, -x) - \mathcal{U}(a, x)(\mathcal{U}(a, -x))' = \mathcal{U}'(a, x)\mathcal{U}(a, -x) + \mathcal{U}(a, x)\mathcal{U}'(a, -x), \tag{3.70}
$$

where the prime here denotes the derivative with respect to the second argument; therefore (3.69) demands that the Wronskian of $\mathcal{U}(B^2+A, x)$ and $\mathcal{U}'(B^2+A, -x)$ must vanish at $x = 2iB$. Since both $\mathcal{U}(B^2+A, x)$ and $\mathcal{U}(B^2+A, -x)$ are solutions to the parabolic cylinder equation

$$
\frac{d^2\mathcal{U}}{dx^2} - \left(\frac{1}{4}x^2 + B^2 + A\right)\mathcal{U} = 0, \tag{3.71}
$$

the Wronskian must be a constant due to Abel's identity[1]. Therefore if the Wronskian of $\mathcal{U}(B^2+A, x)$ and $\mathcal{U}'(B^2+A, -x)$ were to vanish at $x = 2iB$, it must vanish at $x = 0$ as well. In other words,

$$
\mathcal{U}(B^2+A, 0)\mathcal{U}'(B^2+A, 0) = 0. \tag{3.72}
$$

With the formulae for $\mathcal{U}$ and $\mathcal{U}'$ at the origin from Bender & Orszag (1999), as well as noting that that the Gamma function $\Gamma(z)$ diverges when z is zero or a negative

---

[1] Abel's identity states that for a linear second order differential equation $y'' + p(x)y' + q(x)y = 0$, the Wronskian is given by $C \exp\left(-\int p(x)dx\right)$. For the parabolic cylinder equation $p(x) = 0$, and hence the Wronskian is a constant.

integer, we have:

$$\mathcal{U}(B^2 + A, 0) = 0 \iff \frac{3}{4} + \frac{1}{2}(B^2 + A) = 0, -1, -2, -3 \cdots,$$

$$\mathcal{U}'(B^2 + A, 0) = 0 \iff \frac{1}{4} + \frac{1}{2}(B^2 + A) = 0, -1, -2, -3 \cdots,$$

where $\mathbb{N}$ and $\mathbb{Z}$ denotes the set of natural numbers and the set of integers respectively. Together these two conditions imply $B^2 + A = -\left(-\frac{1}{2} + n\right)$, where $n \in \mathbb{N}$. Reverting back to the original variables, we find that the correction to the eigenvalue is:

$$\gamma_1 = -\left(\frac{2n - 1}{2}\right)\sqrt{\frac{2}{\upsilon}} - \frac{l_{3/2}^2}{4} \tag{3.73}$$

The prediction for the eigenvalue is therefore:

$$\gamma = \upsilon + \epsilon\gamma_1 = \upsilon - (2n - 1)\sqrt{\frac{\mu}{2\upsilon}} - \frac{l^2}{4\mu} \tag{3.74}$$

Therefore the fastest growing mode corresponds to $n = 1$, which in turn gives $\mathcal{U}'(B^2 + A, 0) = \mathcal{U}'(-1/2, 0) = 0$.

To complete our analysis, we will need to determine the constant r in the inner solution. Note that $\hat{R}_1(Y) = (F_1 + F_2)/2$, and with the aid of (3.68) we can eliminate c_1, leaving one undetermined coefficient for $\hat{R}_1$. In addition, we have not used the conditions $\hat{R}_1(0) = \sqrt[4]{8\upsilon}$ and $\hat{R}_1'(0) = 2\upsilon r$ in (3.65) during our matching; after some algebra, these conditions will give:

$$r = \frac{i\sqrt[4]{8\upsilon}}{2\upsilon}\frac{\mathcal{U}'(-1/2, -2iB)}{\mathcal{U}(-1/2, 2iB)}. \tag{3.75}$$

Notice that $\mathcal{U}(-1/2, x) = e^{-x^2/4}$ satisfies (3.71) (Temme, 2010), and therefore

$$r = -\frac{l_{3/2}}{\sqrt{2\upsilon}}. \tag{3.76}$$

46

3.2.3 Energetics

To explain the unexpected results observed in the previous section, we will examine the energetics associated with the normal modes. If we substitute the normal mode solutions $A_j(y)e^{\gamma - i(\omega - a))t}$ into the energy equations (3.4) and (3.5), we will have:

$$2\gamma|A_1|^2 = -J_{1y} - D_1 + S\,, \tag{3.77}$$

$$2\gamma|A_2|^2 = -J_{2y} - D_2 + S\,. \tag{3.78}$$

Integrating over the entire domain, the equations become:

$$\gamma = \left(-\hat{D}_1 + \hat{S}\right)\Big/2|\hat{A}_1|^2 = \left(-\hat{D}_2 + \hat{S}\right)\Big/2|\hat{A}_2|^2\,, \tag{3.79}$$

where the hatted variables are the integrated values over the entire domain. In addition we have assumed that J_n vanishes as $y \to \pm\infty$ since $|A_n| \to 0$. The energy equation for the normal mode problem simply states that the growth rate of the instability is determined by the difference between energy source due to PSI activity ($\hat{S}$) and energy sink due to dissipation ($\hat{D}_1$). Figure 3.6 shows the results for $\upsilon = 1$ and $l = 0$, where total energy source $\hat{S}$ and total dissipation $\hat{D}_1$ are calculated using the most unstable eigenfuctions, and are normalized by the wave-energy $|\hat{A}_1|^2$. Not surprisingly, the dissipative term $\hat{D}_1$ (green dots) increases as the dissipation increases; at the same time, the energy source $\hat{S}$ (blue dots) also decreases significantly (20 % compared to the inviscid case), indicating that dissipation also disrupts the energy transfer. At higher dissipation a significant portion of the energy ($\approx 50\%$) generated via PSI is dissipated away.

The results for $l = 0.1$ is plotted in figure 3.7. For larger dissipation, the situation is very similar to the $l = 0$ case: The total dissipation $\hat{D}_1$ increases significantly while the energy source $\hat{S}$ drops. On the other hand, as $\mu \to 0$ the system
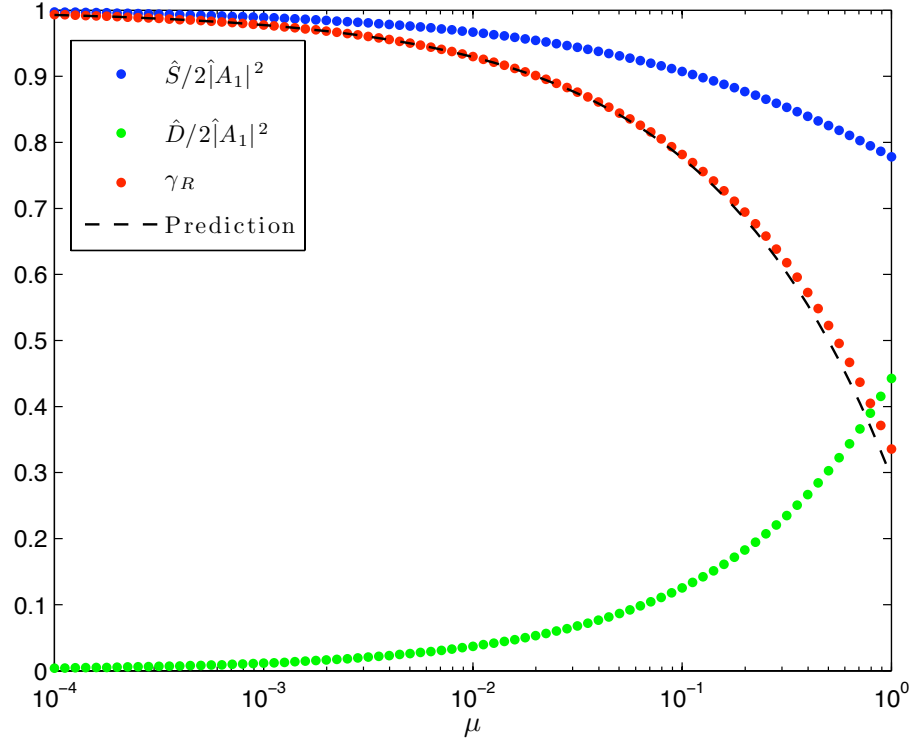
Figure 3.6: *Energetics of PSI: $l = 0$.* $\hat{S}$ (blue dots) and $\hat{D}_1$ (green dots) from (3.79) are calculated and normalized by using the eigenfunctions, and are plotted here as a function of μ. The numerically computed growth rate (red dots) and the asymptotic prediction from (3.74) (dashed line) are also plotted for comparison. $\upsilon = 1$ and $y_L = -200$.
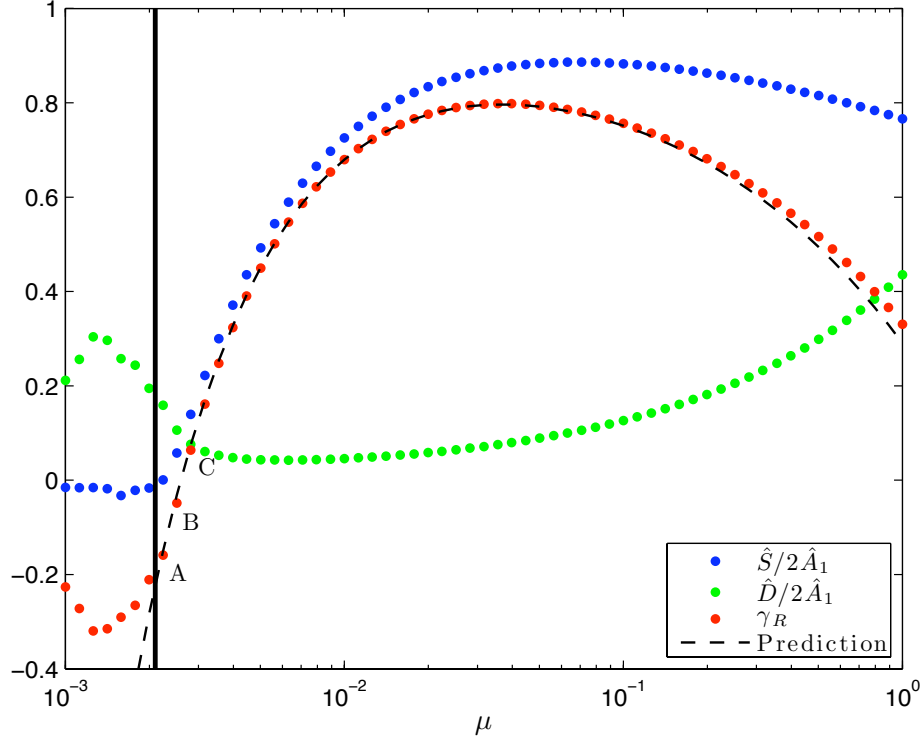
Figure 3.7: *Energetics of PSI: $l = 0.1$. $\hat{S}$ (blue dots) and $\hat{D}_1$ (green dots) from (3.79)
are calculated and normalized by using the eigenfunctions, and are plotted here as a
function of μ. The numerically computed growth rate (red dots) and the asymptotic
prediction from (3.74) (dashed line) are also plotted for comparison. The vertical
line separates the boundary modes and the localized modes. $\upsilon = 1$ and $y_L = -1500$.*

behaves very differently compared to the $l = 0$ case: when μ drops below 10^{-2}, the
energy source $\hat{S}$ drops off rapidly while the energy dissipation $\hat{D}_1$ increases. These
two effects combine to stabilize the system when the dissipation is sufficiently small.

To further understand the stability problem in the small dissipation limit,
we will now examine the energetics more closely. If we integrate (3.77) from y to
∞,

$$\int_y^\infty S(s)ds = \int_y^\infty D_1(s)ds + 2\gamma \int_y^\infty |A_1(s)|^2 ds - J_1(y), \qquad (3.80)$$

49

(3.80) states that total energy generated via PSI to the north of y is either dissipated, converted into PSI wave, or transported out of the region between y and ∞. (which is represented by $J_1(y)$. We will consider the three modes that are close to the stability boundary ($\gamma_R = 0$) with dissipation $\mu_1 = 0.002238$, $\mu_2 = 0.002512$, and $\mu_3 = 0.002818$; these modes correspond to the growth rates marked by A, B, and C respectively in figure 3.7. The four terms in (3.80) are computed using the eigenfunctions (normalized such that $\max(|A_1|) = 1$) and are plotted in 3.8 together with the eigenfunction.

From the plot of $|A_1|^2$ in panel a, we can see clearly that the waves become more and more de-localized as μ decreases; the eigenfunctions are very similar near the turning latitude, but the eigenfunction for μ_3 (blue curve) decays significantly faster than the eigenfunction for μ_1 (red curve). A plot of $\int_y^\infty |A_1(s)|^2 ds$ (panel b) illustrates the delocalization more precisely: the energy density integral for μ_3 becomes constant when $y \approx -120$, while for μ_1 it converges only when $y < -280$.

Earlier we saw that the dissipation increases as μ decreases, and the plot of energy flux J_1 in panel c provides a possible explanation: as μ decreases, the meriodional energy flux becomes more negative, meaning that more energy is transported southwards by the PSI waves. As the waves become increasingly oscillatory to the south, dissipation is more effective since it increases with the wave-number. Thus in this regime the energy generated near the critical latitude is transported to the south where it is dissipated away, and the end result is that the global dissipation increases despite a decrease in the dissipation parameter.

The other phenomenon we have observed earlier is that the overall energy source via PSI $\hat{S}$ also decreases with μ. $\int_y^\infty S(s) ds$ is plotted in panel (e) of figure 3.8, which demonstrates how the source term changes over the domain. For μ_3

50

(blue curve), it first increases rapidly as we move south and away from the turning point, indicating there is significant energy input near the critical latitude. For μ_2 (green curve), the integral increases much slower near the critical latitude compared to the previous case, and therefore energy input via PSI is greatly reduced. When μ further decreases to μ_3, the integral becomes negative near the turning latitude, showing that the energy is in fact being drained from the PSI waves into the pump wave. The integral continues to decrease as we head south until $y = -50$, where a minimum is reached and the integral starts to increase; thus the source term is positive to the south of $y = -50$, and energy is transfered from the pump-wave into the PSI waves. The net transfer of energy $\hat{S}$ is small as the drain of energy to the north is balanced by the gain of energy to the south.
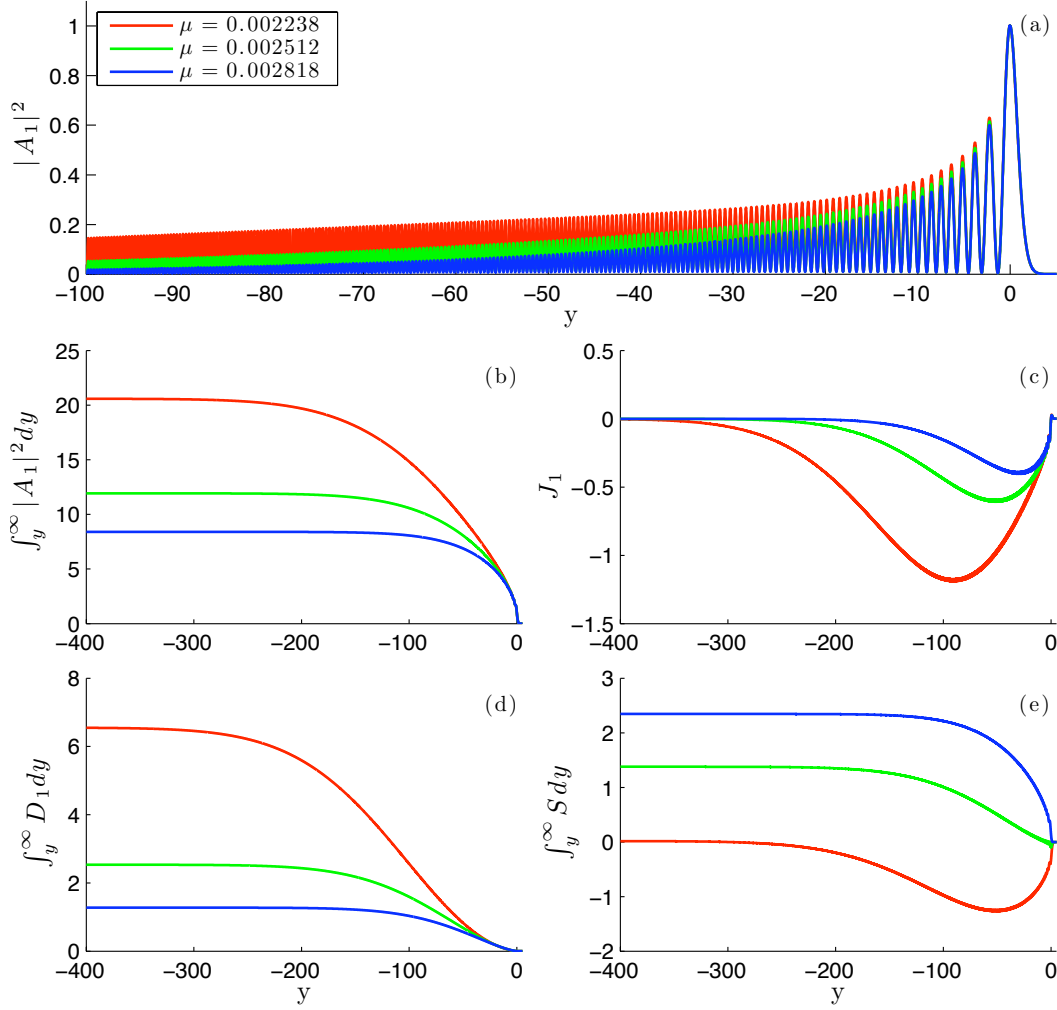
Figure 3.8: *Energetics of PSI near the stability boundary.* The eigenfunctions for $\mu = 0.002238$ (red), $\mu = 0.002512$ (green), and $\mu = 0.002818$ (blue) are used to compute the various terms in the energy equation (3.80). (a) $|A_1|^2$. (b) $\int_y^\infty |A_1(s)|^2 ds$. (c) J_1. (d) $\int_y^\infty D_1(s) ds$. (e) $\int_y^\infty S(s) ds$. $\upsilon = 1$ and $y_L = -1500$. Please note that the range for the horizontal axis in (a) is $-100 < y < 5$ but the range for (b) to (e) is $-400 < y < 5$.

3.3 More initial value problems

A couple of Initial value problems will now be presented to further illustrate some of the properties of our PSI model discussed in §3.2.

3.3.1 Transient growth

Figure 3.9 shows the result of an initial value problem where $v = 2$, $l = 0.5$, $\mu = 0.028$. The computational domain is $[-200, 50]$, with a PML located between $[-200, 185]$. The normal mode analysis shows that the system is asymptotically stable, as the eigenvalue calculation shows the maximum growth rate to be $\gamma_R = -0.3267$. The initial perturbation is in the form of a Gaussian wave packet:

$$A_1(y, 0) = e^{-(y+25)^2/5} \cos(\sqrt{26}y), \quad A_2(y, 0) = 0 \tag{3.81}$$

In the top panel of figure 3.9, $|A_1|$ is plotted for $0 \leq t \leq 2.5$ and $-80 \leq y \leq 5$. As in the example shown in §3.1, the wave packet splits into two components that travel in opposite directions; between the wave packets, the wave amplitude experiences a growth due to PSI. This growth continues exponentially, and the wave amplitude increases from $O(1)$ to $O(10^5)$ by $t = 20$ (see the second panel); the growth comes to an end at $t \approx 20$, and the wave amplitude subsequently decays exponentially at a rate that is consistent with the eigenvalue analysis. In figure 3.10 the wave amplitude $|A_1|$ at various times are plotted, which illustrates the transient growth more clearly.

The numerical result suggests that a very significant transient growth is possible, even though the system is asymptotically stable. We will be examining transient growth in much greater detail in §4.3.2.

53

3.3.2 Boundary modes

The second example is one where a boundary mode eventually dominates the numerical solution. In figure 3.11, the amplitude of the wave $|A_1|$ is plotted at various times for $v = 2$, $l = 0.1$ and $\mu = 10^{-4}$; the computational domain is similar to the previous example. Panel (a) shows the initial perturbation given by a Gaussian wave packet centred at $y = -75$:

$$A_1(y, 0) = e^{-(y+75)^2/5} \cos(\sqrt{75}y), \quad A_2(y, 0) = 0 \, . \tag{3.82}$$

The initial dynamics is similar to the previous example, where an exponentially growing mode is excited between the wave packets (panels (b) to panel (f)); the difference however is that the mode eventually gives way to an exponentially growing boundary mode that dominates the solution (panels (g) to (l)). Note that the wave profile appears to be solid due to the rapid oscillations, which are well resolved by the grid used in the numerical computation. As in the normal mode anlysis in §3.2.1, the type of boundary conditions (zero dirichlet, sponge layer or radiative) had minimal effect on the growth rate of the unstable boundary modes in the IVP.
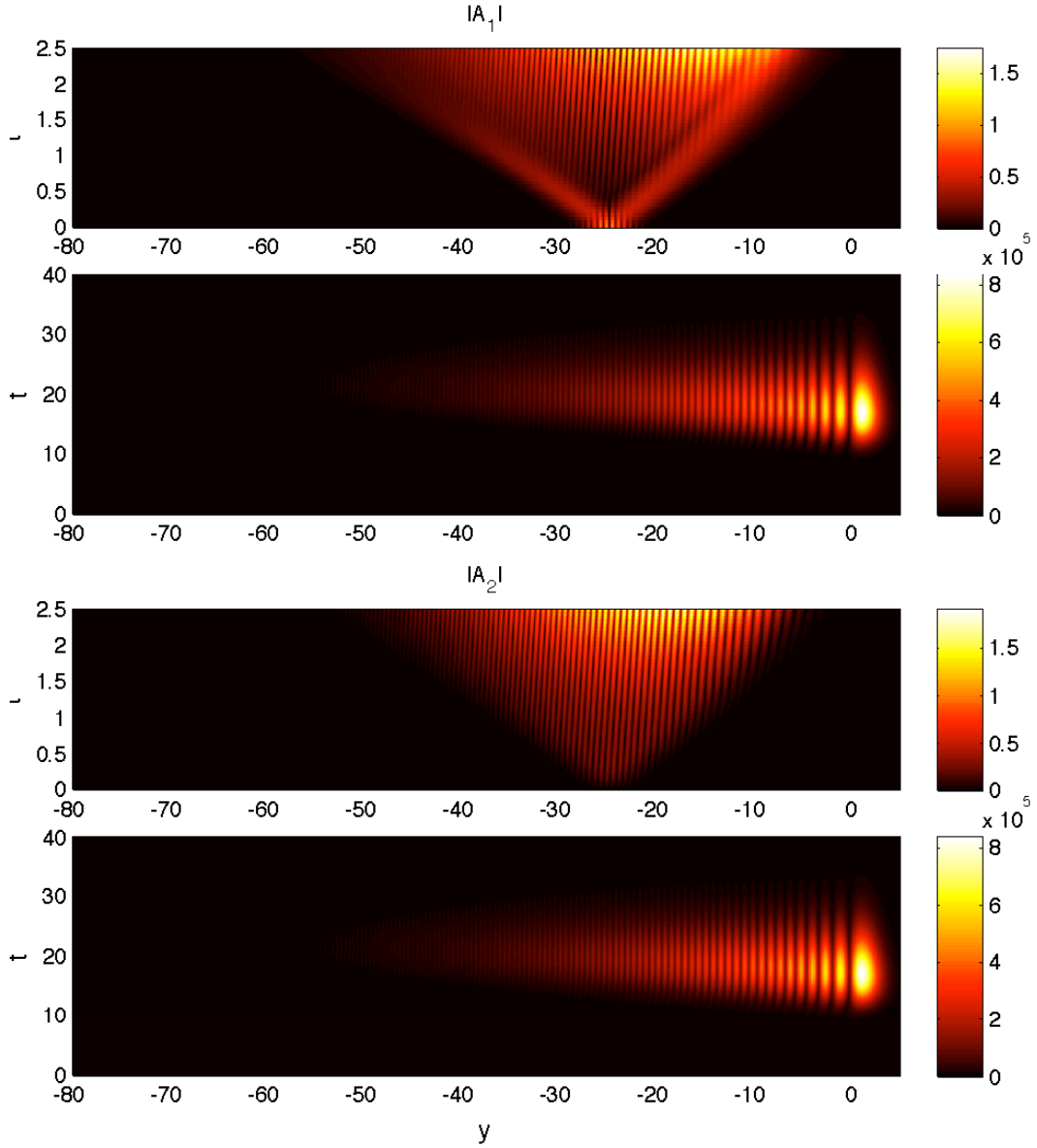
Figure 3.9: *An initial value problem with transient growth* The results from a numerical computation of the PSI model. $|A_1|$ is plotted in the top two panel, with the top panel showing the initial growth from $t = 0$ to 2.5. The second panel shows the entire computation from $t = 0$ to 40. Note that the color scale is different for the two plots. A similar set of plots for $|A_2|$ are produced in the bottom two panels. The parameters used are $v = 2$, $l = 0.5$, and $\mu = 0.028$, with the spatial domain being $[-185, 50]$ and a sponge layer located at $[-200, -85]$. Only the data from $[-80, 5]$ is shown here.

Figure 3.10: *An initial value problem with stable normal modes.* $|A_1|$ at various times are plotted. The parameters used are $\upsilon = 2$, $l = 0.1$, and $\mu = 0.028$, with the spatial domain being $[-185, 50]$ and a sponge layer located at $[-200, -85]$. Only the data from $[-80, 30]$ is shown here.
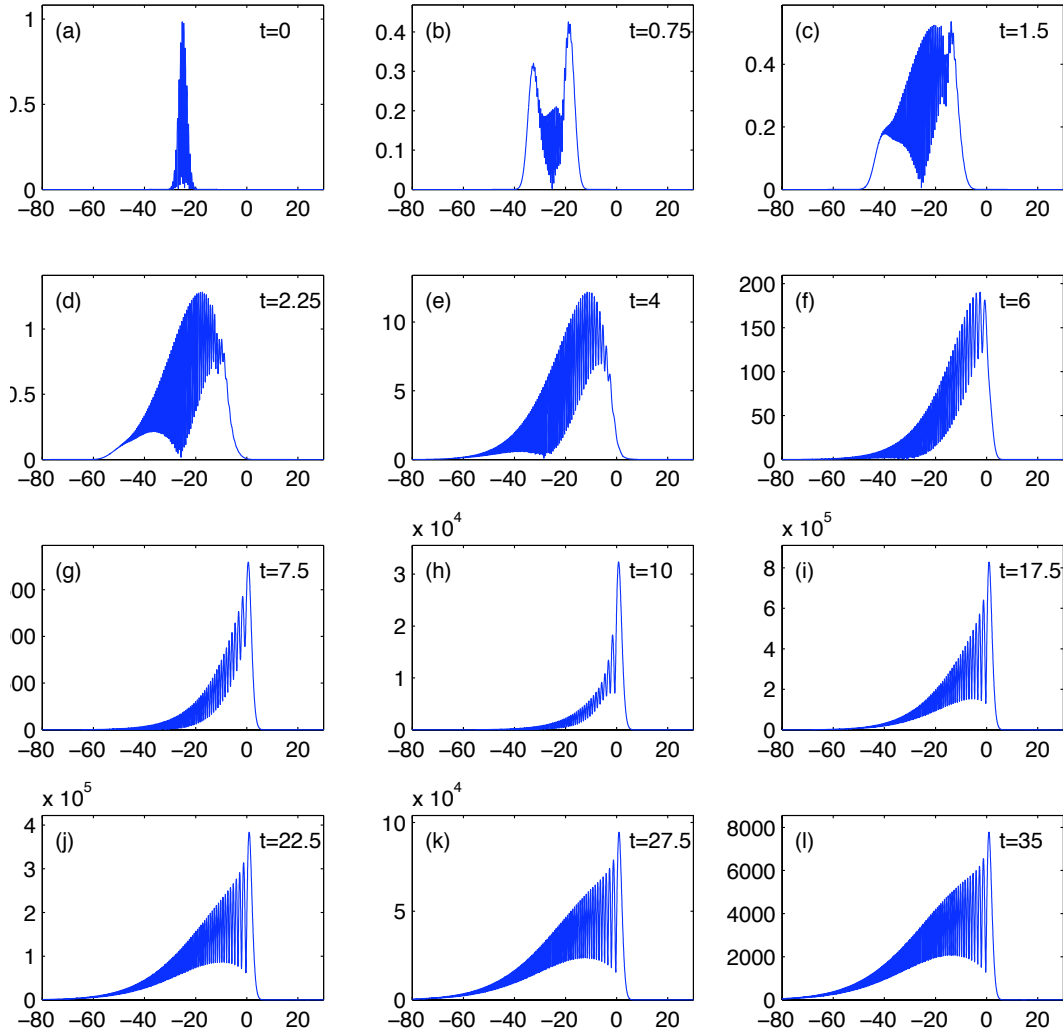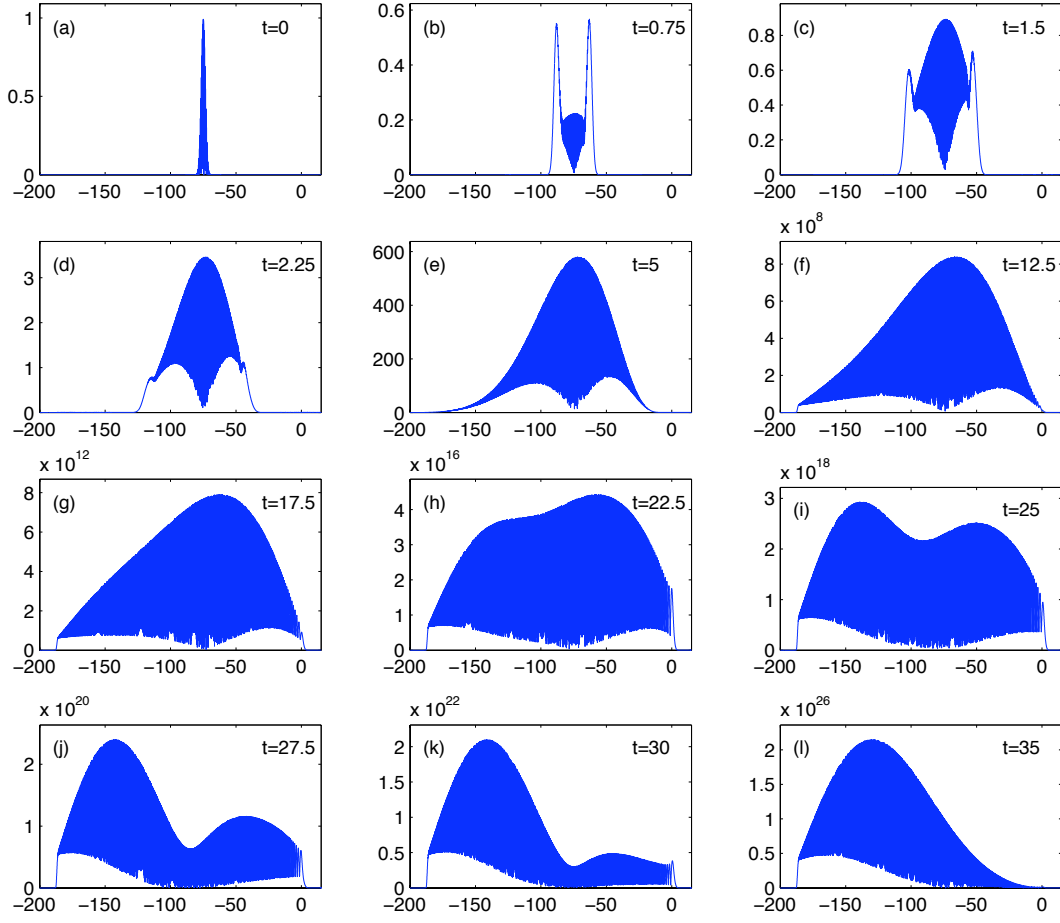
Figure 3.11: *An initial value problem with boundary mode.* $|A_1|$ at various times are plotted here. The parameters used are $\upsilon = 2$, $l = 0.1$, and $\mu = 10^{-4}$, with the spatial domain being $[-185, 50]$ and a sponge layer located at $[-200, -85]$. Only the data from $[-200, 10]$ is shown.

3.4　Summary

In this chapter we have presented an initial value problem in which a perturbation in form of a Gaussian wave packet results in exponential growth, and a normal mode analysis confirms the existence of unstable modes. The stability problem was investigated numerically, as well as analytically in the limit of small dissipation and small pump wavenumber (i.e. $l \ll 1$ and $\mu \ll 1$). When l is non-zero, the unexpected result is a vanishing dissipation has a stabilizing effect, which is confirmed by an initial value problem; however the IVP also showed that a significant transient growth is possible even when the PSI-waves are asymptotically stable. In the next chapter we will explore the transient growth, as well as the stability of the PSI-model in the inviscid limit.

Chapter 4

PSI in the Inviscid Limit

The goal of this chapter is to further understand the PSI model in the inviscid limit. There are two questions we would like to address:

1. *What is the shape of the spectrum for the inviscid problem?* In the previous chapter, as we decreased the dissipation parameter (μ), the spectra eventually became contaminated by unstable boundary modes that have little physical meaning. While the analytical and numerical results suggests that the discrete unstable modes will eventually become stable as $\mu \to 0$, it is not clear if there are other physical modes present.

2. *What is the nature of the large transient growth observed in some initial value problems?* We are interested in understanding the mathematical explanation behind the transient growth in an asymptotically stable system.

4.1 Stability of the inviscid problem

To address the first question, we will solve the inviscid problem analytically via a Fourier transform. Setting μ in (3.18) and (3.19) to zero, the inviscid equations are:

$$A_{1yy} = (y - i\gamma)A_1 + ve^{ily}A_2,\tag{4.1}$$

$$A_{2yy} = (y + i\gamma)A_2 + ve^{-ily}A_1.\tag{4.2}$$

Applying Fourier transform $\mathcal{F}\{\cdot\}$ to the equations, and defining $F(q) = \mathcal{F}\{A_1(y)e^{-ily/2}\}$ and $G(q) = \mathcal{F}\{A_2(y)e^{ily/2}\}$, we have

$$\frac{\mathrm{d}F}{\mathrm{d}q} = i\left(q^2 + \tfrac{1}{4}l^2 + ql - i\gamma\right)F + ivG,\tag{4.3}$$

$$\frac{\mathrm{d}G}{\mathrm{d}q} = ivF + i\left(q^2 + \tfrac{1}{4}l^2 - ql + i\gamma\right)G.\tag{4.4}$$

Note that under Fourier transform, y is transformed into $i\frac{\mathrm{d}}{\mathrm{d}q}$. These equations can be further simplified by a change of variable:

$$\hat{F}(q) = e^{i\left(\frac{1}{3}q^3 + \frac{1}{4}l^2q\right)}F(q) \quad \text{and} \quad \hat{G}(q) = e^{i\left(\frac{1}{3}q^3 + \frac{1}{4}l^2q\right)}G(q).\tag{4.5}$$

(4.3) and (4.4) become:

$$\frac{\mathrm{d}\hat{F}}{\mathrm{d}q} = i(ql - i\gamma)\hat{F} + iv\hat{G},\tag{4.6}$$

$$\frac{\mathrm{d}\hat{G}}{\mathrm{d}q} = iv\hat{F} - i(ql - i\gamma)\hat{G}.\tag{4.7}$$

We can eliminate one of the equations to form a second order ODE. For example, using (4.7) to eliminate $\hat{G}$ in (4.6), we have:

$$\frac{\mathrm{d}^2\hat{F}}{\mathrm{d}q^2} + \left[(lq - i\gamma)^2 + v^2 - il\right]\hat{F} = 0.\tag{4.8}$$

Defining $z \equiv \sqrt{\frac{il}{2}}\left(q - \frac{i\gamma}{l}\right)$ and $H(z) = \hat{F}(q)$ the equation can be manipulated into the standard parabolic cylinder equation:

$$\frac{\mathrm{d}^2H}{\mathrm{d}q^2} - \left[\frac{1}{4}z^2 + \left(-\frac{iv^2}{2l} - \frac{1}{2}\right)\right]H = 0.\tag{4.9}$$

60

In this case the solutions are $\mathcal{U}(a, z)$ and $\mathcal{U}(a, -z)$, where $a = -\frac{iv^2}{2l} - \frac{1}{2}$; their Wronskian is given by (Temme, 2010):

$$W = \frac{\sqrt{2\pi}}{\Gamma(\frac{1}{2} + a)} = \frac{\sqrt{2\pi}}{\Gamma(-\frac{iv^2}{2l})}, \tag{4.10}$$

which will not vanish since the gamma function is finite along the imaginary axis. Thus these two solutions to (4.14) are linearly independent, and form a satisfactory basis.To carryout the inverse Fourier transform, H must remain bounded as $q \to \pm\infty$; however we can demonstrate that this cannot be true if $\gamma_R \neq 0$.

We will first consider $q \to \infty$. In this case $\arg z \approx \pi/4$, and the asymptotic formula for $|z| \gg 1$ is given by (Temme, 2010):

$$\mathcal{U}(a, z) \sim e^{-\frac{1}{4}z^2} z^{-a-1/2} + O(1/z^2). \tag{4.11}$$

Now since

$$z^2 = \frac{il}{2}\left(q^2 - 2\frac{i\gamma}{l}q - \frac{\gamma^2}{l^2}\right) = \frac{il}{2}\left(q^2 - \frac{\gamma^2}{l^2}\right) + \gamma q, \tag{4.12}$$

$e^{-z^2/4}$ will be bounded as $q \to \infty$ if and only if $\gamma_R \geq 0$. On the other hand, as $q \to -\infty$, $\arg z \approx -3\pi/4$, and the appropriate asymptotic formula is

$$\mathcal{U}(a, z) \sim e^{-\frac{1}{4}z^2} z^{-a-\frac{1}{2}} - i\frac{\sqrt{2\pi}}{\Gamma(\frac{1}{2} - a)} e^{i\pi a} e^{\frac{1}{4}z^2} z^{a-\frac{1}{2}} + O(1/z^2). \tag{4.13}$$

In this case the first term contains $e^{-z^2/4}$, which will increase without bounds unless $\gamma_R \leq 0$. Combining the two constraints, we arrive at the conclusion that $\gamma_R = 0$ for $\mathcal{U}(a, z)$ to be bounded. For the other solution $\mathcal{U}(a, -z)$, a similar analysis will lead to the same conclusion.

Therefore for if H is to remain bounded as $q \to \pm\infty$, $\gamma_R = 0$. What the analysis above suggests is that for the inviscid problem, there are no unstable normal modes. On the other hand, both $\mathcal{U}(a, z)$ and $\mathcal{U}(a, -z)$ remains bounded whenever γ is purely imaginary. Thus a continuous spectrum of eigenvalues exists, and the corresponding eigenfunction can be obtained by reversing the Fourier transform.

4.2 Non-normal operators and transient growth

Traditionally in fluid mechanics, the hydrodynamical stability is considered through normal mode analysis, where infinitesimally small perturbations can grow exponentially into finite amplitude disturbances for unstable flows. The growth rates for the normal modes are given by the eigenvalues, while the spatial structure is described by the eigenfunctions. Normal mode analysis have been quite successful for problems such as the Rayleigh-Bèrnard instability and Taylor-Couette instability, as experimental and analytical prediction for instability agree (Trefethen *et al.*, 1993). However for shear flows such as plane Couette and Poiseuille flows, the onset of turbulence occurs at Reynolds number much lower than the threshold predicted by theory (Trefethen *et al.*, 1993; Butler & Farrell, 1992). For example, Couette flows are theoretically stable for all Reynolds numbers, but transition to turbulence was observed in laboratory at Reynolds number of ≈ 360 (Tillmark & Alfredsson, 1992). For plane Poiseuille flow, the critical Reynolds number unstable normal modes for the Orr-Sommerfeld equation is $Re > 5772.22$ (Orszag, 1971), while transition to full turbulence was observed for Re as low as 1000 (Carlson *et al.*, 1982).

Since the 1990's, the limitation of the normal mode analysis was gradually recognized. It turns out that for a problem where the operator is 'normal' (i.e. the eigenfunctions are orthogonal), the behaviour of the system is completely determined by the spectra. The linear operators in the Rayleigh-Bèrnard and Taylor-Couette stability problems fall into this category, and therefore the normal mode analysis succeeded in predicting the onset of instability (Trefethen *et al.*, 1993). In contrast, the Orr-Sommerfeld operator for shear instabilities is in fact 'non-normal', in the sense that the eigenfunctions are not orthogonal. A consequence of non-orthogonal eigenfunctions is that while the long term behavior of a system is dictated by the

spectra, these systems can have significant transient growth, which the normal mode analysis fails to capture.

4.2.1 A simple example

The following example was used by Farrell & Ioannou (1996) to illustrate some of the features of non-normal operators. Consider a simple 2×2 matrix:

$$A = \begin{bmatrix} -1 & -\cot\theta \\ 0 & -2 \end{bmatrix}, \qquad (4.14)$$

A matrix M is defined to be normal if $MM^\dagger = M^\dagger M$, where † denotes the Hermitian transpose[1]. Here we have

$$AA^\dagger - A^\dagger A = \begin{bmatrix} \cot^2\theta & \cot\theta \\ \cot^2\theta & 0 \end{bmatrix}, \qquad (4.15)$$

and therefore A is normal only if $\theta = \pi/2$, and becomes increasingly non-normal as $\theta \to 0$. It turns out that the non-normality can play an important role in the transient behaviour of a dynamical system. Farrell & Ioannou (1996) considered the following dynamical system:

$$\frac{d\mathbf{x}}{dt} = A\mathbf{x}. \qquad (4.16)$$

The matrix A has eigenvalues $r = -1$ and $r = -2$ with eigenvectors $\mathbf{v}_1 = (1, 0)$ and $\mathbf{v}_2 = (\cos\theta, \sin\theta)$, and the general solution is given by:

$$\mathbf{x} = c_1 e^{-t} \begin{bmatrix} 1 \\ 0 \end{bmatrix} + c_2 e^{-2t} \begin{bmatrix} \cos\theta \\ \sin\theta \end{bmatrix}. \qquad (4.17)$$

Consequently all solutions are asymptotically stable (i.e. $\mathbf{x} \to 0$ as $t \to \infty$ for all initial conditions $\mathbf{x}_0$), with decay rate -1. Farrell & Ioannou (1996) continued on

---

[1]A Hermitian transpose is also known as the conjugate transpose

to demonstrate that an asymptotic stability analysis does not capture the dynamics of the system as $\theta \to 0$. In this limit, $\mathbf{v}_2 \to \mathbf{v}_1$, and the eigenvectors become almost parallel to each other. The ramification is that if the initial condition is almost orthogonal to these eigenvectors, c_1 and c_2 have to be large and have opposite signs in order for the initial condition to be satisfied. For example, the solution with initial condition $\mathbf{x}_0 = (\sin\theta, -\cos\theta)$, which is orthogonal to $\mathbf{v}_2$, will be given by $c_1 = \sin\theta + \cos\theta \cot\theta = \csc\theta$ and $c_2 = -\cot\theta$; clearly in this case as $\theta \to 0$, c_2 decreases without bound, and $c_1 \to -c_2$. The solution to the initial value problem is

$$\mathbf{x} = e^{-t}\begin{bmatrix} \csc\theta \\ 0 \end{bmatrix} + e^{-2t}\begin{bmatrix} \sin\theta - \csc\theta \\ -\cos\theta \end{bmatrix}. \tag{4.18}$$

Now as t increases, the second term will quickly vanish, while the first term can have a magnitude much greater than unity if θ is small. As $|\mathbf{x}_0| = 1$, this indicates that the amplitude experiences a significant growth before decaying. To further illustrate this, notice that the solution to (4.16) with initial condition $\mathbf{x}(0) = \mathbf{x}_0$ can be written as:

$$\mathbf{x} = e^{At}\mathbf{x}_0, \tag{4.19}$$

If we restrict ourselves to initial conditions that satisfies $|\mathbf{x}_0| = 1$, then

$$\max |\mathbf{x}| = \max_{|\mathbf{x}_0|=1} |e^{At}\mathbf{x}_0| = ||e^{At}||, \tag{4.20}$$

where $||\cdot||$ denotes the induced matrix 2-norm. $||e^{At}||$ is therefore a measure of the maximum magnitude of $\mathbf{x}$. In figure 4.1, $||e^{At}||$ for $\theta = \pi/2, \pi/4, \pi/10$, and $\pi/100$ are plotted as a function of time. For all four cases, the curves all become a straight line with slope -1 in accordance with the asymptotic stability analysis. The main difference is that for $\theta = \pi/2$, which corresponds to A being a normal matrix, the solution decays with a decay rate of -1 for all t. On the other hand, as θ decreases
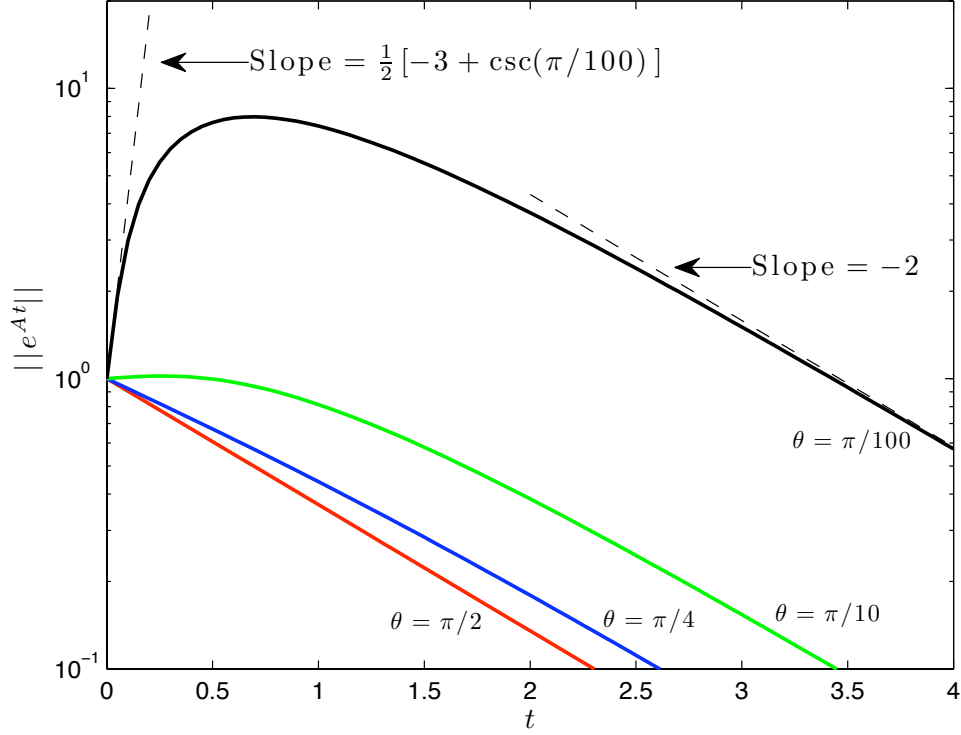
Figure 4.1: *Transient growth for a simple dynamical system.* $||e^{At}||$ is plotted for four values of θ: $\theta = \pi/2, \pi/4, \pi/10$, and $\pi/100$, where A is defined in (4.14). Also plotted as dash line is the initial growth rate give by $\frac{1}{2}(-3 + \csc\theta)$, and the asymptotic decay rate -1 for $\theta = \pi/2$. Note that the vertical axis is in logarithmic scale.

to $\pi/4$ and $\pi/10$, A becomes increasingly non-normal, and the decay in $||e^{At}||$ is delayed. For $\pi/100$, the difference is even more remarkable, as $||e^{At}||$ increased almost an order of magnitude before decaying. The initial growth rate near $t = 0$ is given by the maximum eigenvalue of $(A + A^\dagger)/2$, which in this case is $\frac{1}{2}(-3 + \csc\theta)$ (Farrell & Ioannou, 1996). This suggests that for positive initial growth the criterion is $\theta < \pi/9.244$. From figure 4.1, we can see that for $\theta = \pi/10 < \pi/9.244$, $||e^{At}||$ indeed increases slightly near $t = 0$. For $\theta = \pi/100$, the curve for $||e^{At}||$ agrees well with the predicted initial growth rate of $\frac{1}{2}(-3 + \csc\pi/100)$.

65

4.2.2 Non-normal operators and fluid dynamics

This simple example in the previous section illustrates that while the dynamics of a normal system can be characterized by the eigenvalues, they do not capture the transient behaviour for non-normal systems. This fact was demonstrated clearly in a study by Reddy *et al.* (1993) where the Orr-Somerfeld operator in the Poiseuille problem was analyzed; for a Reynolds number in the stable regime, the energy increased by a factor of 51 before the perturbation decayed away. Similarly, Butler & Farrell (1992) investigated the optimal excitation of perturbations in a plane Couette flow, and found energy amplifications of $O(1000)$ despite Couette flow being stable. The implication of these findings is that transient growth can amplify small perturbations and trigger the transition to turbulence without the need to normal mode instability. Non-normal operators also received attention in the geophysical fluid dynamics community in recent years, for example in the studies of baroclinic instability, error amplification in weather forecast, El Niño, and the stability of thermohaline circulation (Farrell & Ioannou, 1996; Trefethen & Embree, 2005, Ch. 23, and references therein).

4.3 Pseudospectra and PSI

4.3.1 Pseudospectra

Properties of a non-normal operator/matrix can be characterized by the pseudospectra. For $\epsilon \geq 0$, the ϵ-*pseudospectra* of matrix A, $\sigma_\epsilon(A)$, is defined as the set of $z \in \mathbb{C}$ such that z is an eigenvalue of $A + E$ for some perturbation matrix $||E|| \leq \epsilon$ (Reddy *et al.*, 1993). For normal operators, a perturbation to the matrix A of size $||E|| \leq \epsilon$ will perturb the spectra of A, $\sigma(A)$, by a distance no more than ϵ. On the other

hand, for a non-normal matrix the eigenvalues can be perturbed much larger than the perturbation to the matrix (Reddy *et al.*, 1993). The pseudospectra has to be computed numerically for most cases, and it provides a convenient way to visualize the degree of non-normality of an matrix operator.

One important information that can be extracted from the pseudospectra is the lower bound to the maximum of $||e^{At}||$. Suppose that $\alpha_\epsilon(A)$ is the supremum of the real part of $\sigma_\epsilon(A)$, then the following inequality holds:

$$\sup_{t\geq 0}||e^{At}|| \geq \alpha_\epsilon(A)/\epsilon\,. \tag{4.21}$$

Since (4.2) holds for all $\epsilon \geq 0$, a good estimate for the lower bound is the Kreiss constant, which is defined as

$$\mathcal{K}(A) = \sup_{\epsilon\geq 0}\alpha_\epsilon(A)/\epsilon\,, \tag{4.22}$$

which leads to

$$\sup_{t\geq 0}||e^{At}|| \geq \mathcal{K}(A)\,. \tag{4.23}$$

For details, please see Reddy *et al.* (1993) or Chapters 14 ad 15 in Trefethen & Embree (2005).

4.3.2 Transient growth

We will now consider our stability problem in the context of pseudospectra. Re-writing (3.1) and (3.2),

$$A_{1t} = -i\left[-(1-i\mu)A_{1yy} + yA_1 + ve^{ily}A_2\right], \tag{4.24}$$

$$A_{2t} = -i\left[(1+i\mu)A_{2yy} - yA_2 - ve^{-ily}A_1\right]. \tag{4.25}$$

(4.24) and (4.25) can be written as a dynamical system:

$$\frac{d\vec{A}}{dt} = -iM\vec{A}\,, \tag{4.26}$$

where M is the matrix resulting from a spatial discretization. In this section we are going to discretized the spatial derivative using a spectral collocation (or pseudo-spectral) method using Chebyshev polynomial as interpolant (see Weideman & Reddy (2000) or Trefethen (2000) for more details). While the resulting matrix is dense compared to the finite difference scheme used in chapter 3, its smaller size allow for the use of `eig` in MATLAB to compute the full set of eigenvalues; in addition it results in much better convergence in the calculation of the pseudospectra. We have compared the spectra for the same set of parameters using the same method, and they agree over the region of interest.

In §3.3.1, we have seen that for $\upsilon = 2$, $l = 0.5$, and $\mu = 0.028$, the PSI waves grew significantly before decaying as predicted by the normal mode analysis, and we would like to investigate this transient growth with the aid of the pseudospectra associated with the spatial operator. The pseudospectra for the corresponding matrix M is calculated using the `eigtool` package[2] for MATLAB. Due to the extra factor of $-i$ in (4.26), we will have to consider the imaginary part of the spectrum and pseudospectra for information pertaining to growth. In figure 4.2, we can see that all eigenvalues (black dots) lie below the real axis, and therefore the normal modes are stable, confirming the long term behaviour exhibited by the IVP in §3.3. On the other hand, the pseudospectra protrudes significantly above the real-axis, indicating that the discretized matrix M is highly non-normal. By considering $\sigma_\epsilon(M)$ for $\epsilon = 10^{-3}$, we can see that a perturbation of $O(10^{-3})$ results in an $O(1)$ shift in the eigenvalues. Since the operator is non-normal, the transient growth we have observed in the IVP should not be surprising.

We will now take a closer look at the transient growth in the corresponding
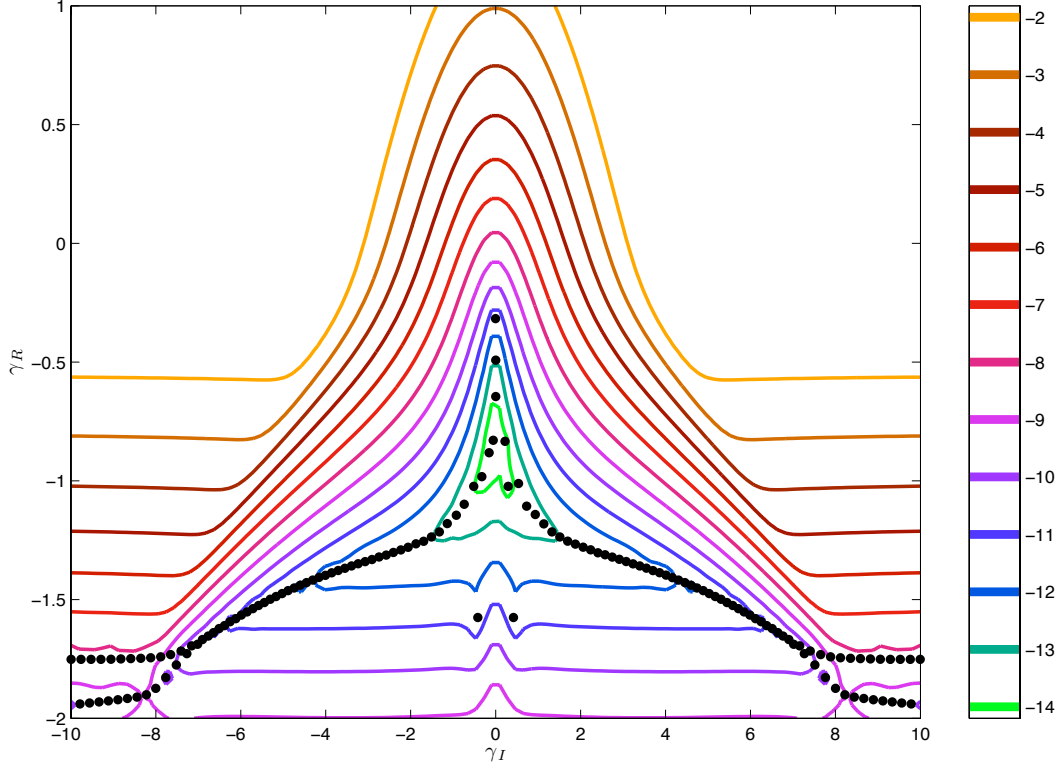
---

[2]Thomas G. Wright. EigTool. `http://www.comlab.ox.ac.uk/pseudospectra/eigtool/`, 2002.

Figure 4.2: *Pseudospectra for a stable system.* The ϵ-pseudospectra for the discretized spatial operator M for (4.24) and (4.25) is plotted (from top to bottom) as level curves for $\epsilon = 10^{-2}, 10^{-3}, \ldots 10^{-14}$. The eigenvalues are plotted as black dots.

IVP by considering the total energy contained in the PSI waves:

$$E_{tot}(t) = \int_{-\infty}^{\infty} (|A_1| + |A_2|) \, dy \qquad (4.27)$$

In figure 4.3, E_{tot} (normalized so that the $E_{tot}(0) = 1$) is plotted as a function of time (blue curve). We can see that the energy increased to almost 10^{13} times the initial energy before the decay sets in at a rate predicted by the eigenvalues (dashed black line). The magnitude of growth is consistent with the lower bound given by (4.21): from figure 4.2, the ϵ-pseudospectra for $\epsilon = 10^{-7}$ have a maximum imaginary part of 0.187, and therefore the lower bound for the maximum growth of $||e^{At}||$ will

be 1.87×10^6, which is equivalent to an increase in energy by a factor of $\approx 3.5 \times 10^{12}$. This estimation is plotted in figure 4.3 as the blue dotted line, which shows that the observed amplification is in line with the prediction given by the pseudo spectra.

In figure 4.3, E_{tot} for $\mu = 0.033$ (green curve) and $\mu = 0.038$ (red curve) are also plotted for comparison. The dissipation parameter μ appears to only have a minor effect on the transient growth rate; the onset of transient growth is delayed slightly for $\mu = 0.038$, but in all three cases the transient growth is exponential with comparable growth rates. The transient growth continues pass $t > 15$, before the growth/decay predicted by the normal mode analysis sets in.

The growth rate for E_{tot} in the transient phase is estimated to be ≈ 2.6, whereas the asymptotic growth rates are -0.65, 0.015, and 0.50 respectively for $\mu = 0.028$, 0.033, and 0.038. This indicates that the transient growth plays a significant role in the evolution of the PSI-waves, particularly in cases where the normal modes are neutral or stable; even when unstable normal modes are present, the transient growth can still occur at a significantly shorter time scale compared to the asymptotic growth.

We will present a plot to illustrate the dependence of transient growth on the initial condition. In figure 4.4, we have plotted E_{tot} for five different initial configurations (see table 4.1). We have not explored in depth the optimal excitation that leads to the maximum transient growth, but from the figure we can notice that the wave-number of the perturbation affects the transient growth significantly.

The physical significance of our result is that transient growth, rather than unstable normal modes, appears to be the dominant force in the excitation of PSI-waves in certain regimes; even in cases where the PSI-waves are asymptotically stable, the transient growth may be sufficiently large for a transition into a non-
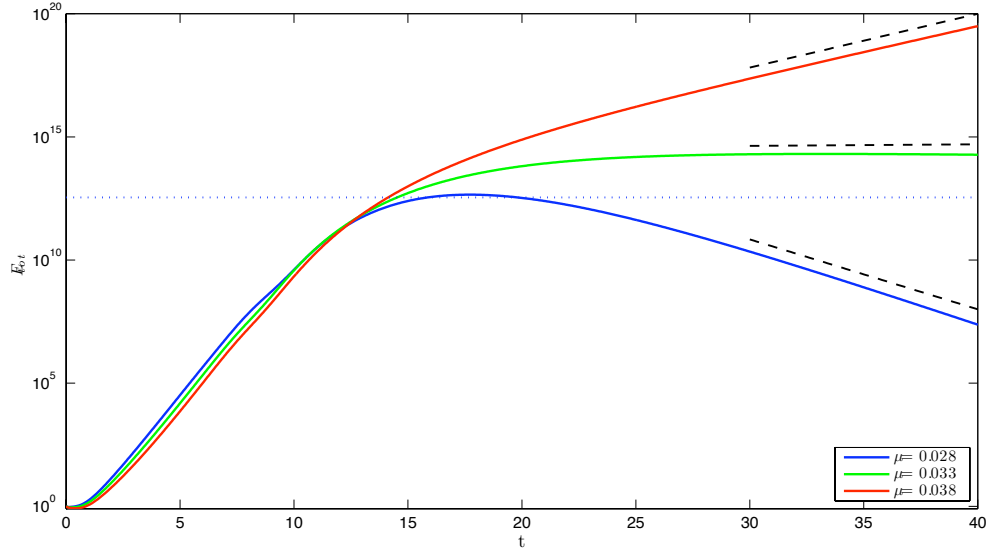
70

Figure 4.3: *Transient growth in a time dependent problem.* The total energy for the IVPs considered in §?? are plotted as a function of time. The black dashed lines on the right are the asymptotic growth/ decay predicted by the eigenvalues, while the blue dotted line is the minimum growth predicted by the pseduospectra.
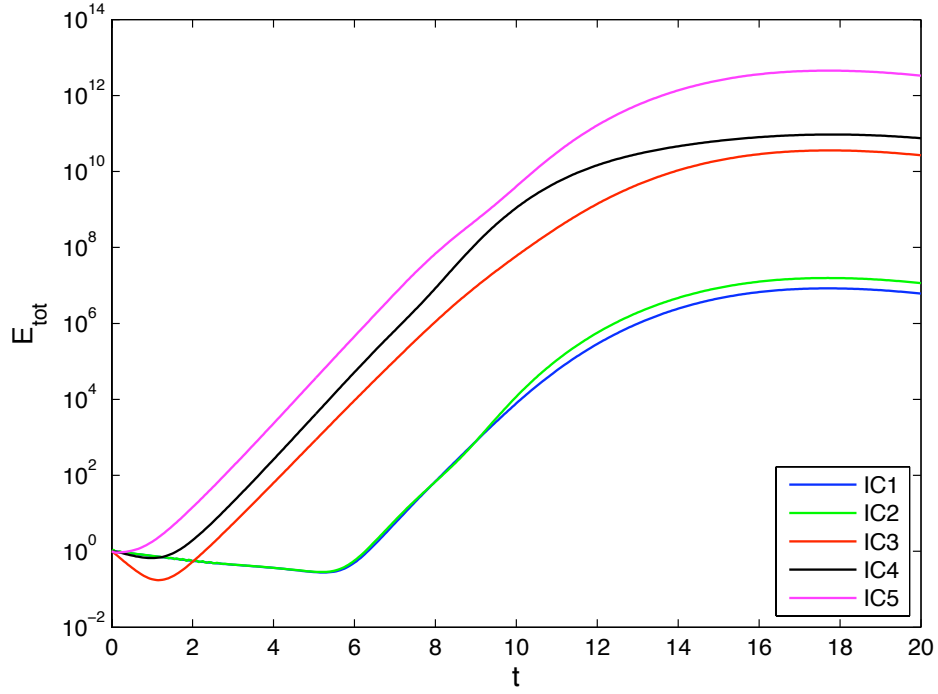
linear regime.

Figure 4.4: *Initial condition and transient growth.* The total energy E_{tot} for different initial conditions are plotted as a function of time. $\upsilon = 2$, $l = 0.5$, and $\mu = 0.028$.

Table 4.1: Initial conditions for figure 4.4

	$A_1(y,0)$	$A_2(y,0)$
IC1	$e^{-(y+25)^2/5}\cos(\sqrt{5}y)$	0
IC2	$e^{-(y+25)^2/5}\cos(\sqrt{5}y)$	$\mathrm{i}e^{-(y+25)^2/5}\cos(\sqrt{5}y)$
IC3	$e^{-(y+25)^2/5}\cos(\sqrt{40}y)$	0
IC4	$e^{-(y+25)^2/5}\cos(\sqrt{15}y)$	0
IC5	$e^{-(y+25)^2/5}\cos(\sqrt{25}y)$	0

4.3.3 Numerical difficulties

The non-normality in operators/matrices also results in complications during numerical computations of eigenvalues, since the operator is sensitive to errors; the round off errors act as a perturbation to the matrix, and if the operator is non-normal, the perturbation is sufficient to shift the eigenvalues. An example of the round-off errors can be detected in figure 4.2; near the center of the plot where the three branches meet, the eigenvalues are not symmetric about the imaginary axis, and they are sensitive to slight changes in the domain length.

Reddy *et al.* (1993) considered the Airy operator

$$\frac{\mathrm{i}}{Re}\frac{d^2}{dy^2} + y\,, \tag{4.28}$$

as a model for the Orr-Sommerfeld operator in shear-flow instabilities. The spectra of the Airy operator consists of three branches in a 'Y'-shape, which resembles the spectrum in figure 4.2. Reddy *et al.* found the operator to be non-normal, and the eigenvalues near the intersection were difficult to compute as they were sensitive to perturbations; the sensitivity increased with as the Reynolds number Re increased. Notice that the Airy operator is in fact part of the spatial operator in our PSI-model, and $Re \to \infty$ in Reddy *et al.* corresponds to $\mu \to 0$ in our model. Thus in hind sight, we should not be surprised by the non-normality of our eigenvalue problem in the inviscid limit.

The effect of round-off error is much more evident in figure 4.5, where the eigenvalues for discretized operator with $v = 6$, $l = 1.5$ and $\mu = 0.1$ are computed using two different level of precision. In the right panel, the eigenvalues are calculated using double precision floating point, and we can see that the eigenvalues line up along the boundary of the pseduospectra with $\epsilon = 10^{-14}$. In the left panel, the

eigenvalues for the same matrix were computed with single precision; the eigenvalues near the center now lie along the pseudospectra for $\epsilon = 10^{-6}$. At the same time, the eigenvalues in the lower left and right regions of the spectra are very similar for the two computations, showing that a change in numerical precision did not affect the accuracy significantly for these parts of the spectra.

When the non-normality becomes severe, the round-off error prevents the eigenvalues near the center from being calculated accurately. The growth rate predicted by our asymptotic theory in §3.2.2 (c.f. (3.74)) for $v = 6$, $l = 1.5$ and $\mu = 0.1$ is 0.346. In panel (b) of figure 4.5, the predicted eigenvalue of 0.346i is right in the middle of the area enclosed by the eigenvalues perturbed due to round-off error. Due to the severe non-normality, the true eigenvalue cannot be resolved even by the `eigs` command in MATLAB.

This effect of non-normality is the most prominent in the transition region between the boundary modes in the inviscid limit to the localized modes. The example considered above is marked in panel (b) of figure 3.5 by A. As the largest γ_R reported by the eigenvalue calculation near A is the perturbed eigenvalue due to the round-off error rather than the true eigenvalue, the growth rate is potentially overestimated. This explains why the numerically calculated growth rate agrees with the prediction for larger values of μ, but they break off suddenly from the prediction when μ becomes too small. By computing the pseudospectra near the breaking point for decreasing values of μ, we have confirmed that the round off error starts affecting the eigenvalue with the largest growth rate precisely at the breaking point in the plot.

The non-normality of the matrix also affected the use of iterative schemes, such as the `eigs` function in MATLAB, for the computation of eigenvalues. In
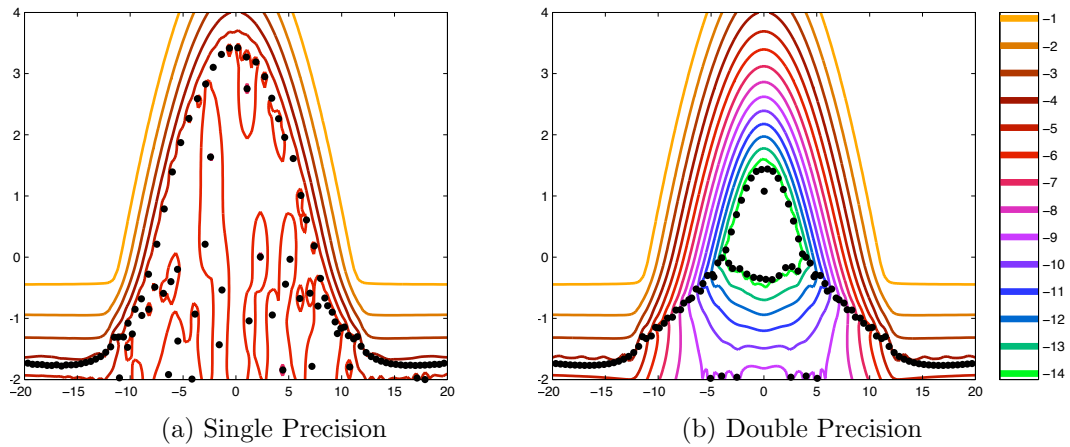
(a) Single Precision	(b) Double Precision

Figure 4.5: *Effect of non-normality on the calculation of eigenvalues* The eigenvalues computed for $\upsilon = 6$, $l = 1.5$ and $\mu = 0.1$ for (a) single precision floating point, and (b) double precision floating point.

particular, when the eigenvectors become almost linearly dependent, the convergence in such iterative schemes can be significantly slowed (Trefethen & Embree, 2005); this has been a problem for our calculations, especially in the invisicid limit. An additional complication is that even when the iterations converge, the estimated eigenvalues (Ritz values) are not guaranteed to be close to the actual eigenvalues (Trefethen & Embree, 2005). Indeed in the inviscid limit we encountered difficulty in using `eigs` to compute the eigenvalues as the convergence was slow.

4.4   Summary

In this chapter we considered the stability of the inviscid PSI problem, and concluded that there are no unstable normal modes. In addition, as $\mu \to 0$, the spatial operator in our model becomes non-normal. A consequence of the non-normality is that a significant transient growth can occur with suitable perturbations, and the transient

growth can in fact dominate the dynamics of PSI. Therefore in the inviscid limit, the PSI model may best be understood via its transient dynamics, rather than the traditional modal instability.

Chapter 5

Discussion

5.1 Horizontal dissipation

In this thesis, we have formulated a linear model for PSI, and explored its behaviour in Chapter 3. Solving the PDE numerically as an initial value problem revealed the presence of exponentially growing normal modes, which suggest that the PSI problem can be formulated in a normal mode stability analysis. The main result is that for a meridionally propagating pumpwave (i.e. $l \neq 0$), instability can only occur when the horizontal eddy viscosity μ_H is sufficiently large. Through the analysis of the energy equation, the stability in the inviscid limit can be attributed to two factors. A reduction in μ_H increases the meridional energy flux towards the equator, which prevents a build up of energy in the PSI waves near the critical latitude. At the same time the energy transfer from the pump wave to the PSI waves is also less effective.

The β-effect and the dissipation together limit the horizontal extent of PSI. As the PSI-waves are near-inertial at the critical latitude of $28.9°$, the decrease in Coriolis force to the south implies that the horizontal wave number must increase,

and therefore the wave energy is dissipated away more rapidly to the south. This provides an alternative mechanism to the localization of PSI seen in MacKinnon & Winters (2005), where the localization was attributed to a vertical divergence in energy flux preventing a build up of energy to the south of the critical latitude.

Depending on the horizontal scale, the horizontal eddy diffusivity measured from dye-release experiments ranges from 10^{-2} m^{2}s^{-1} for a horizontal scale of 0.1km to 10^3m^{2}s^{-1} at a scale of 1000km (Ledwell *et al.*, 1998). The intermediate values of $10^0 - 10^1$m^{2}s^{-1} correspond to $\mu \sim 10^{-2} - 10^{-1}$ since the eddy diffusivity is scaled by $\lambda^3\beta = 1.36 \times 10^2$m^{2}s^{-1}. For this range of μ, our model predicts that the PSI activity will be localized to between 15-30 units, or 300-600km, to the south of the critical latitude (c.f. figure 3.3 for example). For comparison, the Hawaiian Islands, which is a strong site for generation of mode-1 internal tides, lies between 19.5°N to 22°N, or approximately between 750 to 1000 km south of the critical latitude. Thus the meridional extent of PSI imposed by horizontal eddy diffusion can be significant compared to other length scales, such as the source location for the pump-wave.

For an near-intertial wave, we can demonstrate that the horizontal eddy diffusivity is significant compared to vertical eddy diffusion. For a plane wave, the horizontal and vertical eddy diffusion can respectively be characterized by $\mu_H(k^2+l^2)$ and $\mu_V m^2$. We wish to consider the ratio between the two quantities. Using the dispersion relation for an internal wave with the near-inertial approximation $\omega = f_0$, $f = f_0 + \beta y$, and $N \gg f$

$$\frac{\mu_H(k^2 + l^2)}{\mu_V m^2} = \frac{\mu_H}{\mu_V}\frac{\omega^2 - f^2}{N^2 - f^2} \approx \frac{\mu_H}{\mu_V}\frac{-2f_0\beta y}{N^2} . \tag{5.1}$$

Taking $\mu_V = 10^{-5}$m^{2}s^{-1}, $\mu_H = 10$m^{2}s^{-1} and the parameters from table 2.1, the

last term in (5.1) is:

$$\frac{\mu_H(k^2 + l^2)}{\mu_V m^2} = \frac{-y}{27\text{km}} \tag{5.2}$$

What this tells us is that near the origin, the vertical dissipation is much larger than the horizontal dissipation, which is expected since near the critical latitude, the vertical structure of near-inertial waves is much finer than the horizontal structure; however as the wave packet moves south, the horizontal wave number increases, and at 27km south of the critical latitude the horizontal dissipation is the same order of magnitude as the vertical dissipation. This justifies the include of the horizontal dissipation in our model.

In summary, while horizontal dissipation was included originally as a cure for numerical issues (boundary modes), it is clear that it is in fact dynamically significant for an near-inertial wave on the β-plane.

The normal mode problem of our PSI model is also interesting from a mathematical perspective. We were able to calculate the exact solution to the eigenvalue problem with $\mu = l = 0$, where a continuous spectrum of unstable modes are possible when $\upsilon > 0$. On the other hand, while a continuous spectrum of eigenfunctions also exists for the inviscid problem with $\mu = 0$ but $l \neq 0$, the eigenfunctions are all stable. This suggests that $\mu = l = 0$ is a singular limit as we cannot recover the solutions by taking $l \rightarrow 0$. The inviscid solutions appear to be singular as well since the growth rate of the discrete normal modes in the dissipative problem tends to $-\infty$ as $\mu \rightarrow 0$.

5.2 Transient growth

Another interesting mathematical property of our model is the non-normality of the spatial operator. As we approach the inviscid limit, the eigenfunctions for the operator become parallel to each other, which caused difficulties in our numerical computations for eigenvalues. A closer look at our spatial differential operator revealed connections to the Orr-Sommerfeld operator for the stability problem in plane Poiseuille and Couette flows, and the Airy operator, which are all non-normal.

One of the ways the non-normality manifests itself in a time dependent problem is through transient growth. Through a series of initial value problems, we have demonstrated that transient growth is indeed possible, despite the system being asymptotically stable. Even in cases where the system is asymptotically unstable, the transient growth rate is in fact much higher than the growth rate for the unstable normal modes.

The amplitude and wavelength of the pump-wave considered in YTB corresponds to $v \approx 3$ and $l \approx 1$ with our scaling. With $10^{-2} < \mu < 10^{-1}$, the PSI is in the regime where the growth rate increases with dissipation (c.f. panel (a) of figure 3.3). For $\mu = 0.05$, the normal modes are all stable, yet the pseudo-spectra indicates the possibility of large amplitude transient growth (see figure 5.1). The implication is that the transient growth we observed may be oceanographically relevant; transient growth may be the mechanism via which a transition into non-linear regime takes place, rather than via normal mode instability.
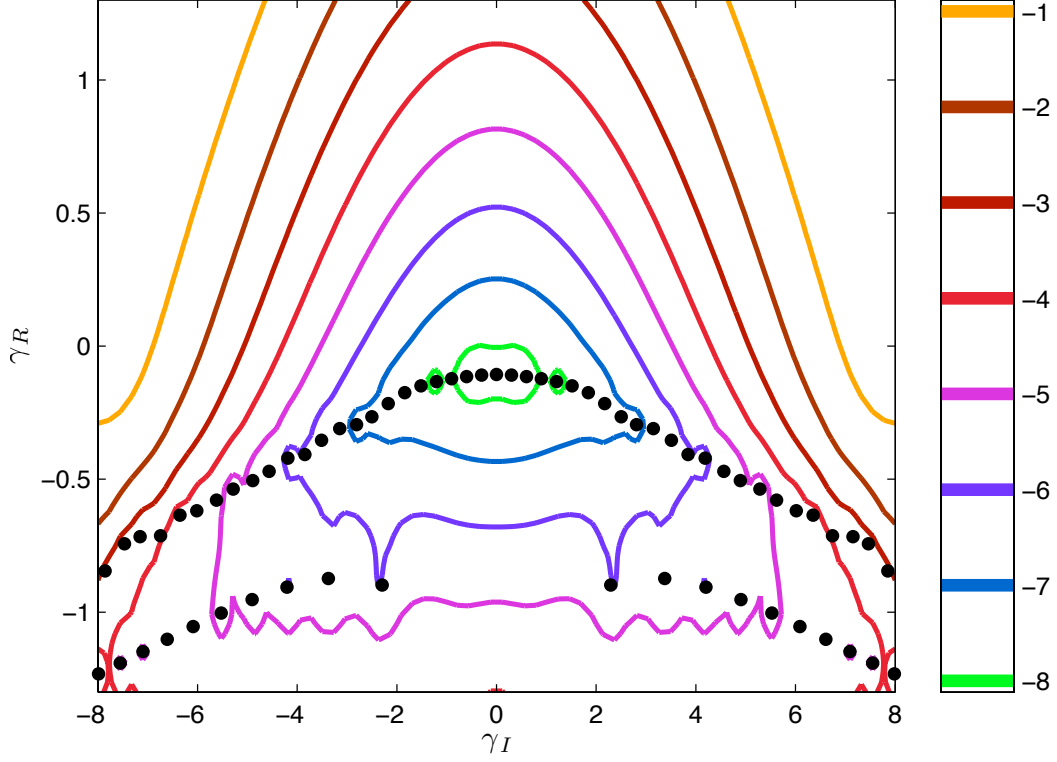
Figure 5.1: *Pseudospectra for a stable system.* The ϵ-pseudospectra for $\upsilon = 3$, $l = 1$, and $\mu = 0.05$ are plotted as level curves for $\epsilon = 10^{-1}$, 10^{-3}, ... 10^{-8}. The eigenvalues are plotted as black dots. The operator is discretized using a spectral collocation method using Chebyshev polynomials as interpolant over the domain $[-75, 75]$

5.3 Outstanding issues

In this thesis we have established that dissipation plays an important role in the stability of PSI. However a number of key questions remain:

1. *What are the implications of a realistically stratified ocean?*

    Through-out this thesis we have assumed a linearly stratified ocean, and the vertical structure of the PSI wave and that of the pump wave are assumed to be independent. Further more, the pump-wave is assumed to be a plane wave.

A more realistic profile for the ocean is the Gill's profile, where the ocean is modeled by a mixed layer with uniform density near the surface, and the density increases smoothly below the mixed layer (Gill, 1984). Mathematically, the buoyancy frequency is given by:

$$N(z) = \begin{cases} 0 & \text{if } 0 \leq z \leq h_{mix} \\ N_0/(z - z_0) & \text{if } z \geq h_{mix} \end{cases} \tag{5.3}$$

The internal-tides associated with this profile can be solved analytically, and these can be used in place of the planar pump-wave in our model. YTB investigated PSI with the Gill's profile on the f-plane, and found intensification of PSI at the base of the mixed layer. On the other hand, the measurements of Alford *et al.* (2007) found PSI activity extending much deeper into the ocean. By generalizing our model to a realistically stratified ocean, we can perhaps better reproduce the observations.

2. *How is the vertical scale of the PSI-waves determined?*

   Another aspect of PSI that demands clarification is the vertical scale selection. The numerical results of MacKinnon & Winters (2005) and the field data of Alford *et al.* (2007) both suggest that PSI favours a particular vertical scale. In the current model the vertical wavenumber m is a scaling parameter, and therefore it is not clear immediately whether vertical scale selection occurs.

3. *What is the optimal excitation for transient growth?*

   For parameters that are oceanographically relevant, our analysis earlier indicated the potential for significant transient growth. We have also demonstrated that the transient growth depends strongly on the initial perturbation.

Therefore to fully understand PSI in the ocean, we must understand the relationship between the perturbation and the subsequent transient growth.

4. *When does non-linearity become dynamically important?*

Both YTB and the current study is based on the linear model of PSI, but It is clear in our model that perturbations are either transiently or asymptotically unstable, and small perturbations can be amplified to the point where a constant amplitude for the pump-wave is no longer valid. In addition the main motivation for the study of PSI is to understand the energy transfer out of internal tides, which requires a model with genuine three-mode coupling that is similar to (1.7) to (1.9). Our linear model essentially takes the form:

$$i\frac{\partial A_1}{\partial t} + \text{propagation terms} = \Upsilon A_2 \,, \tag{5.4}$$

$$i\frac{\partial A_2^*}{\partial t} + \text{propagation terms} = \Upsilon A_1^* \,, \tag{5.5}$$

which is similar to the three mode model of Bretherton (1964). In the derivation of our PSI model (chapter 2), the evolution equation for the pump-wave can be derived if we allow the background variables to vary on the slow time scale. We expect the third equation to take the form of:

$$i\frac{\partial \Upsilon}{\partial t} + \text{propagation terms} = A_1 A_2 \,. \tag{5.6}$$

The fully non-linear equations will allow us to explore a wider range of problems and resolve some outstanding issues. One important issue is the discrepancy between the catastrophic loss of energy from the internal tide in the numerical model of MacKinnon & Winters (2005), and the more moderate loss measured by Alford *et al.* (2007); while the results of YTB and our study suggests that the time-scale over which the instability occurs is oceanographically

83

relevant, one must study non-linear effects such as saturation of the instability and the feedback on the pump-wave to fully understand the PSI in the ocean.

Bibliography

ABRAMOWITZ, MILTON & STEGUN, IRENE A. 1964 *Handbook of mathematical functions with formulas, graphs, and mathematical tables*, *National Bureau of Standards Applied Mathematics Series*, vol. 55. For sale by the Superintendent of Documents, U.S. Government Printing Office, Washington, D.C.

ALFORD, M. H, MACKINNON, J. A, ZHAO, ZHONGXIANG, PINKEL, ROB, KLYMAK, JODY & PEACOCK, THOMAS 2007 Internal waves across the pacific. *Geophysical Research Letters* **34** (24), 6.

BENDER, CARL M. & ORSZAG, STEVEN A. 1999 *Advanced mathematical methods for scientists and engineers. I*. New York: Springer-Verlag, asymptotic methods and perturbation theory, Reprint of the 1978 original.

BERENGER, J.P 1994 A perfectly matched layer for the absorption of electromagnetic-waves. *Journal of Computational Physics* **114** (2), 185–200.

BRETHERTON, F. P 1964 Resonant interactions between waves. the case of discrete oscillations. *Journal of Fluid Mech* **20**, 457–479.

BUTLER, KM & FARRELL, B 1992 Three-dimensional optimal perturbations in viscous shear flow. *Physics of Fluids A* **4** (8), 1637–1650.

CARLSON, D. R., WIDNALL, S. E. & PEETERS, M. F. 1982 A flow-visualization study of transition in plane Poiseuille flow. *Journal of Fluid Mechanics* **121**, 487–505.

CARTER, G & GREGG, M 2006 Persistent near-diurnal internal waves observed above a site of m 2 barotropic-to-baroclinic conversion. *Journal of Physical Oceanography* **36**, 1136–1146.

DICKEY, JO, BENDER, PL, FALLER, JE, NEWHALL, XX, RICKLEFS, RL, RIES, JG, SHELUS, PJ, VEILLET, C, WHIPPLE, AL & WIANT, JR 1994 Lunar laser ranging- a continuing legacy of the apollo program. *Science* **265** (5171), 482–490.

EGBERT, GD 1997 Tidal data inversion: Interpolation and inference. *Progress in Oceanography* **40** (1-4), 53–80.

EGBERT, GD & RAY, RD 2000 Significant dissipation of tidal energy in the deep ocean inferred from satellite altimeter data. *Nature* **405** (6788), 775–778.

EGBERT, GD & RAY, R 2001 Estimates of m 2 tidal energy dissipation from topex/poseidon altimeter data. *Journal of Geophysical Research* **106** (C10), 22475–22502.

FARRELL, B & IOANNOU, P 1996 Generalized stability theory. part i: Autonomous operators. *Journal of the Atmospheric Sciences* **53** (14), 2025–2040.

GARCIA, ALEJANDRO L. 1999 *Numerical Methods for Physics (2nd Edition)*. Upper Saddle River, NJ, USA: Prentice-Hall, Inc.

GARRETT, C 2003 Internal tides and ocean mixing. *Science* **301** (5641), 1858–1859.

GARRETT, CHRIS & KUNZE, ERIC 2007 Internal tide generation in the deep ocean. *Annual Review of Fluid Mechanics* **39**, 57–87.

GARRETT, C & MUNK, W 1972 Space-time scales of internal waves. *Geophysical & Astrophysical Fluid Dynamics* **3** (1), 225.

GARRETT, C & MUNK, W 1975 Space-time scales of internal waves: A progress report. *Journal of Geophysical Researchophys. Res.* **80** (3), 291–297.

GILL, A. E. 1984 On the behavior of internal waves in the wakes of storms. *Journal of Physical Oceanography* **14** (7), 1129–1151.

HASSELMANN, K 1966 Feynman diagrams and interaction rules of wave-wave scattering processes. *Reviews of Geophysics* **4** (1), 1–32.

HASSELMANN, K 1967 Nonlinear interactions treated by the methods of theoretical physics (with application to the generation of waves by wind). *Proceedings of the Royal Society of London. Series A, Mathematical and Physical Sciences* **299** (1456), 77–103.

HIBIYA, T, NAGASAWA, M & NIWA, Y 2002 Nonlinear energy transfer within the oceanic internal wave spectrum at mid and high latitudes. *Journal of Geophysical Research-Oceans* **107** (C11), 3207.

HIBIYA, T, NIWA, Y & FUJIWARA, K 1998 Numerical experiments of nonlinear energy transfer within the oceanic internal wave spectrum. *Journal of Geophysical Research* **103** (C9), 18715–18722.

JEFFREYS, H 1921 Tidal friction in shallow seas. *Philosophical Transactions of the Royal Society of London. Series A* **221**, 239–264.

LAURENT, L St. & GARRETT, C 2002 The role of internal tides in mixing the deep ocean. *Journal of Physical Oceanography* **32**, 2882–2898.

LEDWELL, JR, WATSON, AJ & LAW, CS 1993 Evidence for slow mixing across the pycnocline from and open-ocean tracer-release experiment. *Nature* **364** (6439), 701–703.

LEDWELL, J.R, WATSON, A.J & LAW, C.S 1998 Mixing of a tracer in the pycnocline. *Journal of Geophysical Research-Oceans* **103** (C10), 21499–21529.

MACKINNON, JA & WINTERS, KB 2005 Subtropical catastrophe: Significant loss of low-mode tidal energy at 28.9 degrees. *Geophysical Research Letters* **32** (15), L15605.

McCOMAS, C & BRETHERTON, F 1977 Resonant interaction of oceanic internal waves. *Journal of Geophysical Research-Oceans* **82** (9), 1397–1412.

MILLER, G 1966 The flux of tidal energy out of deep oceans. *Journal of Geophysical Research* **71** (10), 2485–2489.

MÜLLER, P, HOLLOWAY, G, HENYEY, F & POMPHREY, N 1986 Nonlinear interactions among internal gravity waves. *Reviews of Geophysics* **24** (3), 493–536.

MUNK, W. & WUNSCH, C. 1998 Abyssal recipes ii: energetics of tidal and wind mixing. *Deep-Sea Res Pt I* **45** (12), 1977–2010.

OLBERS, D & POMPHREY, N 1981 Disqualifying two candidates for the energy balance of the oceanic internal wave field. *Journal of Physical Oceanography* **11**, 1423–1425.

ORSZAG, S. A. 1971 Accurate solution of the Orr-Sommerfeld stability equation. *Journal of Fluid Mechanics* **50**, 689–703.

PHILLIPS, O. M 1960 On the dynamics of unsteady gravity waves of finite amplitude. i. the elementary interactions. *J Fluid Mech* **9**, 193–217.

PHILLIPS, O. M 1961 On the dynamics of unsteady gravity waves of finite amplitude. ii. local properties of a random wave field. *J Fluid Mech* **11**, 143–155.

RAINVILLE, L & PINKEL, R 2006 Baroclinic energy flux at the hawaiian ridge: Observations from the r/p flip. *Journal of Physical Oceanography* **36** (6), 1104–1122.

RAY, R & MITCHUM, G 1997 Surface manifestation of internal tides in the deep ocean: Observations from altimetry and island gauges. *Progress in Oceanography* **40** (1-4), 135–162.

REDDY, SC, SCHMID, PJ & HENNINGSON, DS 1993 Pseudospectra of the orr-sommerfeld operator. *SIAM Journal on Applied Mathematics* **53** (1), 15–47.

SIMMONS, HARPER L 2008 Spectral modification and geographic redistribution of the semi-diurnal internal tide. *Ocean Model* **21** (3-4), 126–138.

TAYLOR, G 1920 Tidal friction in the irish sea. *Philosophical Transactions of the Royal Society of London. Series A, Containing Papers of a Mathematical or Physical Character* **220**, 1–33.

TEMME, N M 2010 *Digital library of mathematical functions*. National Institute of Standards and Technology.

THORPE, S.A. 2005 *The Turbulent Ocean*. Cambridge University Press.

TILLMARK, N. & ALFREDSSON, P. H. 1992 Experiments on transition in plane Couette flow. *Journal of Fluid Mechanics* **235**, 89–102.

TREFETHEN, L, TREFETHEN, A, REDDY, S & DRISCOLL, T 1993 Hydrodynamic stability without eigenvalues. *Science* **261** (5121), 578–584.

TREFETHEN, LLOYD N. 2000 *Spectral methods in MatLab*. Philadelphia, PA, USA: Society for Industrial and Applied Mathematics.

TREFETHEN, LLOYD N. & EMBREE, MARK 2005 *Spectra and pseudospectra*. The behavior of nonnormal matrices and operators.

WEIDEMAN, J. A. & REDDY, S. C. 2000 A matlab differentiation matrix suite. *ACM Trans. Math. Softw.* **26** (4), 465–519.

YOUNG, W. R, TSANG, Y. K & BALMFORTH, N. J 2008 Near-inertial parametric subharmonic instability. *J Fluid Mech* **607**, 25–49.

ZHENG, C 2007 A perfectly matched layer approach to the nonlinear schrödinger wave equations. *Journal of Computational Physics* **227** (1), 537–556.